JGR Atmospheres

RESEARCH ARTICLE
10.1029/2020JD034465

Sahelian Heat Wave Characterization From Observational Data Sets

D. Bouniol[1], F. Guichard[1], J. Barbier[1], F. Couvreux[1], and R. Roehrig[1]

[1]CNRM, Université de Toulouse, Météo-France, CNRS, Toulouse, France

Key Points:

- Observational data sets are used to statistically document processes involved in spring time heat waves in the Sahel
- Nighttime heat waves are linked to an increase in precipitable water as well as a frequent high aerosol load
- Daytime heat waves are generally associated with cleaner skies; more intense events show in addition a higher amount of precipitable water

Correspondence to:
D. Bouniol,
dominique.bouniol@meteo.fr

Citation:
Bouniol, D., Guichard, F., Barbier, J., Couvreux, F., & Roehrig, R. (2021). Sahelian heat wave characterization from observational data sets. *Journal of Geophysical Research: Atmospheres*, *126*, e2020JD034465. https://doi.org/10.1029/2020JD034465

Received 4 JAN 2021
Accepted 16 MAY 2021

Abstract This paper makes use of spaceborne observational data sets in order to characterize radiative processes involved in spring time heat waves in the Sahel. Spring corresponds to the hottest period of the year, with a high aerosol load, a gradual moistening, and the presence of clouds contributing to greenhouse effect. Heat waves are defined as synoptic events that have a large spatial extent and a duration longer than 3 days. Two types of heat waves are studied: daytime heat waves, detected with the daily maximum temperature and nighttime heat waves, detected with the daily minimum temperature. Daytime heat waves correspond to situations where cloud optical thickness is lower than the climatology and a large number of these situations are also associated with a lower aerosol load and a drier atmosphere. Nighttime heat waves correspond to a moister atmosphere compared to the climatology. In a large fraction of them, an increase in aerosol loading is also observed. This study, only based on observational data sets, highlights the subtle but different radiative balance at play in both types of events.

1. Introduction

Heat waves (HWs) can be defined as rare and long lasting warm anomalies of the near-surface air temperature over an extended area (Perkins, 2015). These events may occur at different times of the year. However, their impacts can be dramatic if they occur at a time in the annual cycle when the temperature is already high. The socioeconomical consequences of such events typically differ depending on whether extreme temperatures are reached during day or night (Hong et al., 2018). Here, we focus on the subtropical African Sahel in spring, which is the hottest period of the year (Fink et al., 2017) and particularly affected by HW occurrence (Fontaine et al., 2013). More broadly, Africa is one of the regions suspected to be strongly affected by the brunt of climate change (Niang et al., 2014).

The climate of West Africa, and in particular of the Sahel, is strongly influenced by the West African Monsoon, which controls the dry and wet seasons. Guichard et al. (2009) and Slingo et al. (2009) documented the annual cycle of various atmospheric components using ground-based observations. They show that the near-surface air temperature reaches its maximum value by the middle of May and that this rise in temperature is accompanied by an increase in specific humidity that begins in March–April. Until this time of the year, the Sahel, which mostly consists of grassland and cropland, remains scarcely vegetated.

The first occurrences of precipitation around mid-June induce a drop in the atmospheric temperature and sign the end of a hot and relatively moist period. The spring increase of low-level water vapor amount is not a regular process but results from a succession of monsoon surges which typically last 3–5 days (Couvreux et al., 2010; Marsham et al., 2016). The effect of the monsoon flow is dual over the Sahel: on the one hand, its incursion cools this hot region through the southerly advection of cooler air, while on the other hand, it increases the amount of water vapor in the lower troposphere, which thus warms the atmosphere through an enhanced greenhouse effect. The Sahel is also characterized by a significant aerosol loading throughout the year (Caton Harrison et al., 2019; Prospero et al., 2002). The analysis of airborne and ground-based observations (Formenti et al., 2008; Haywood et al., 2008; Milton et al., 2008) revealed that the Sahelian aerosol layer mostly consists of mineral dust and biomass burning aerosol (Formenti et al., 2008; Haywood et al., 2008; Milton et al., 2008). In winter, the fire season is maximum, thus leading to a large mass fraction of biomass burning aerosols, while from February, dust dominates (90% in March [Milton et al., 2008]) the aerosol mass fraction north of 8°N (Formenti et al., 2008). Dust uplift occurs in dry, sparsely, or nonvegetated regions (Heinold et al., 2013), when the wind close to the surface exceeds a threshold that depends on land-surface properties such as soil texture and moisture. During the spring period, aerosol emission over

the Sahel is then reinforced by major events of wind erosion occurring over sparsely vegetated surfaces (bare and cropped plots) (Pierre et al., 2014). They are associated with a decrease in incoming shortwave (SW) radiation at the surface (Mallet et al., 2009) that, in turn, induces a decrease in temperature in particular during daytime. In contrast, dust traps longwave (LW) radiation in the low troposphere (Pagès et al., 1988) and thus increases surface air temperature during nighttime. Over bright surfaces, dust induces a warming because its LW effect dominates its SW effect (Balkanski et al., 2007; Yang et al., 2009). These climatological behaviors suggest that the couplings between radiation, water vapor, and aerosols may be at play during several consecutive days and thus contribute to the persistence of high temperatures (Marsham et al., 2016).

HW events are often associated with specific atmospheric dynamical features. For instance, it has been demonstrated that midlatitude HW events depend on the establishment and duration of specific atmospheric dynamical regimes (Cattiaux et al., 2009; Meehl & Tebaldi, 2004; Miralles et al., 2014; Parker, Berry, & Reeder, 2014; Parker, Berry, Reeder, et al., 2014). For the Sahel, similar studies remain limited. Fontaine et al. (2013) identified a mechanism that may favor anomalous heating in the very early spring over the Sahel; it involves Rossby waves causing midtropospheric subsidence over the continent. Such events may also be amplified by local thermodynamical processes such as land-surface interactions, water vapor, cloud, or aerosol feedbacks. Miralles et al. (2014) describe a positive feedback situation between soil moisture, circulation, and temperature, where the depletion of soil moisture induced by a high atmospheric demand leads to strong surface sensible heat fluxes. They stress that a substantial increase in temperature can only be explained by considering the multiday soil memory. The Sahel strongly differs from Western Europe in term of climatological state. Indeed, spring coincides with the last months of the dry season, which has not generally seen any rain event since the last monsoon season, except in case of very rare winter events (Guichard et al., 2009). The soil is thus very dry and sparsely vegetated. Gruhier et al. (2008) and Mougin et al. (2009) show that up to the beginning of May the soil moisture remains close to zero in the Sahel, preventing the mechanism identified by Miralles et al. (2014) to be active. Oueslati et al. (2017) quantified the contribution of sensible heat fluxes to the abnormally heat observed in spring 2010 and found a small contribution to the temperature anomaly. The purpose of this study is precisely to investigate the atmospheric mechanisms involved in the temperature amplification during HW events over the Sahel in spring.

The present study adopts a Eulerian approach in order to analyze the combination of atmospheric processes that helps increasing the temperature at a given place, in contrast to Lagrangian approach like in Quinting and Reeder (2017) who made use of back trajectories to characterize air masses associated with HWs. A particular focus is given to the radiative budget and how key factors such as water vapor, clouds, and aerosols can influence the surface air temperature during HW events. Reanalysis data may be of particular interest for such a purpose since all surface and atmospheric variables are provided at the same time and have been extensively used for this purpose (Fontaine et al., 2013; Oueslati et al., 2017). However, since the surface radiation budget involves humidity, aerosol, and cloud contributions that are not very accurately simulated at this particular place and part of the year (e.g., Agusti-Panareda et al., 2010; Diallo et al., 2017), we exclusively use observational data sets in the present study. In particular, HWs are defined as mesoscale to synoptic-scale phenomena (Barbier et al., 2018) and because of their wide spatial coverage and good repetitivity, we investigate the spaceborne data ability to document several aspects of the radiative budget. Over West Africa, several spaceborne-derived atmospheric parameters (satellite level 3 data) may be available over common temporal period. In order to gain confidence in the obtained results, several of these independent data sets are used together to assess the robustness of processes at play during Sahelian HW. When available in the literature, some indications on the individual product accuracy are given, even if there are generally not specific to the West Africa location for the spring period.

A quantitative assessment of the role of the different atmospheric factors on the thermodynamical profile would require the use of a radiative transfer model. However, the use of such a model needs a careful consideration of the vertical distribution of water vapor, cloud, and aerosol layering that is generally not spatially provided in observational data sets. Radiative properties of cloud that may change from one day to the other needs also to be specified and introduce additional hypothesis. This process can be undertaken in particular in well-documented cases but prevents a climatological approach which is the goal of the present study.

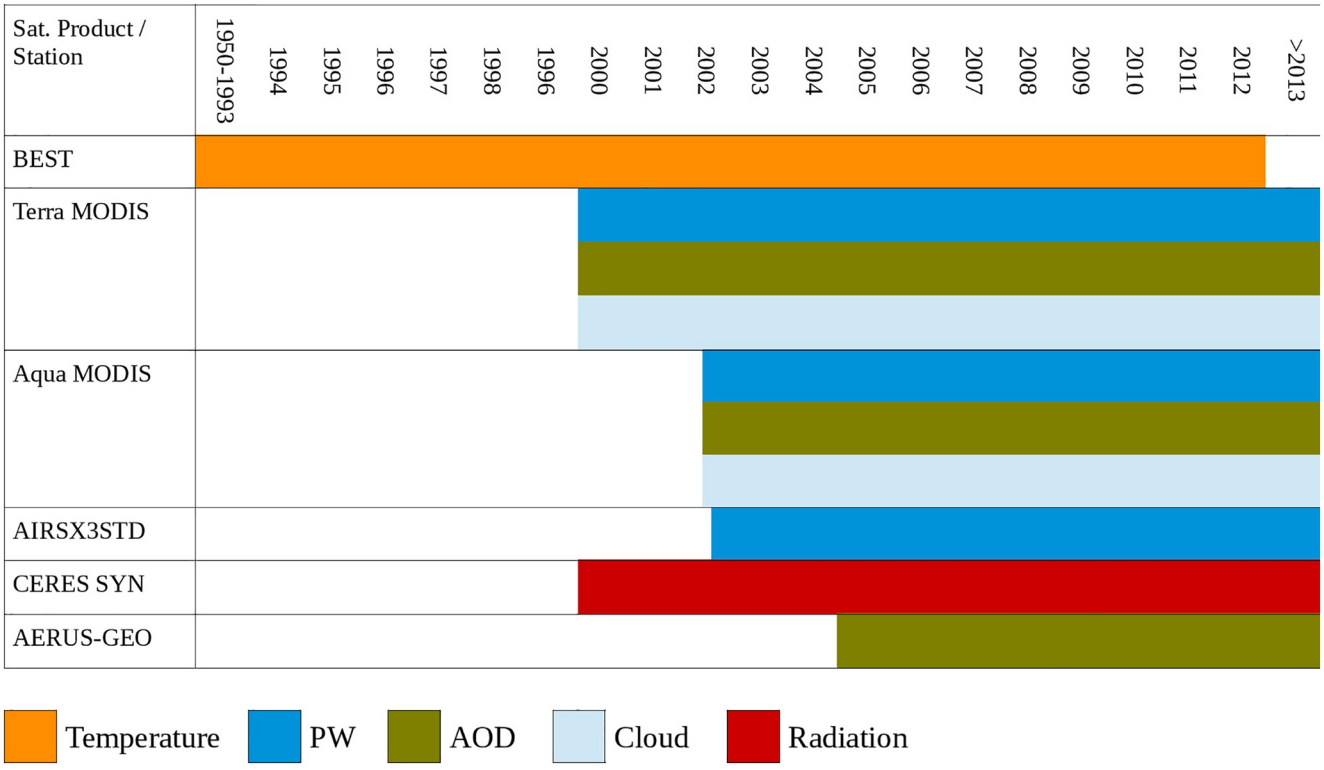

Figure 1. Daily product availability, one color per atmospheric variable.

Section 2 presents the data used in this study and the processing methodology. Because to our knowledge this has not been done yet, the climatological behavior of the different parameters impacting the surface radiation budget is documented in the following section. Section 4 documents the magnitude of atmospheric parameters obtained in case of HWs as well as their anomaly with respect to the climatology and Section 5 analyses their covariations. Concluding remarks are finally given.

2. Data and Methods

The following section presents the various data sets used in this study as well as the implemented strategy used to obtain composites. Only daily products are used in the following.

2.1. Temperature From the Berkeley Earth Surface Temperature Data Set

Two different types of HWs are characterized following the definition of Barbier et al. (2018). They are identified from the daily minimum and maximum temperatures provided in Berkeley Earth Surface Temperature (BEST, Rohde et al., 2013, 2014) gridded data set (see Section 2.7 for the HW identification methodology). This data set is based on daily surface weather records interpolated to equal-area grid cells (with nearly 1.25° resolution at the equator) using Kriging interpolation and then regridded on a 1° × 1° grid-boxes. It covers the 1950–2012 period (see Figure 1) and provides daily minimum temperature (T_{min}), daily maximum temperature (T_{max}), and daily mean temperature (T_{mean}).

Rao et al. (2018) intercompared and evaluated different aspects of four different temperature data sets at monthly time scale and find notable differences at local and regional scales; they attributed these differences to the uneven distribution of the ground stations used to generate the various data sets and to the interpolation methods. Their study suggests that data sets using only station observations have large uncertainties across scales, especially over station-sparse areas. The BEST data set includes more stations than other available products (Rao et al., 2018), explaining why this product is used in the present study over the 1950–2012 period (Figure 1).

2.2. Top of the Atmosphere and Surface Radiative Fluxes From Clouds and the Earth's Radiant Energy System Daily Data

Daily mean radiative fluxes at the Top Of the Atmosphere (TOA) and at the surface are taken from the Clouds and the Earth's Radiant Energy System (CERES) SYN1deg 1° × 1° Ed4 daily products (Rutan et al., 2015). It combines Terra and Aqua CERES radiances (Wielicki et al., 1996), Moderate Resolution Imaging Spectroradiometer (MODIS) cloud (Minnis et al., 2011) and MODIS aerosol observations (Remer et al., 2005), 1-hourly geostationary data to provide hourly broadband TOA radiant fluxes and cloud properties (Doelling et al., 2016), thermodynamical profiles from the Global Modeling and Assimilation Office Goddard Earth Observing System Model reanalysis, and other ancillary data sets related to surface albedo properties (see Table 1 of Rutan et al., 2015). The CERES/MODIS combination onboard Terra (10:30 LT) and Aqua (13:30 LT) are in sun-synchronous orbits, which limits diurnal sampling. The linear interpolation of cloud properties between CERES measurements is not sufficient to estimate the diurnal flux signal in between CERES measurements. Therefore, to estimate the daily mean LW and SW fluxes, the diurnal fluctuations are accounted by incorporating broadband fluxes derived from contiguous geostationary satellite imager radiances between 60°N and 60°S on an hourly basis. Surface radiation calculations are based on a one-dimensional radiative transfer model computing 1-hourly surface radiant flux using reanalysis data for the diurnal cycle of temperature and water vapor amount (Kato et al., 2013). Using a large set of globally distributed ground-based measurements, Rutan et al. (2015) estimate a monthly bias in incoming fluxes at the surface of 3.0 W m^{-2} in the SW and −4.0 W m^{-2} in the LW with 11.6 and 9.7 W m^{-2} standard deviation, respectively. These standard deviations increases up to 31.0 and 19.1 W m^{-2} at the daily time scale. A more specific evaluation based on three Sahel ground-based sites located over a North-South transect and focused on the spring season reveals similar performance for our region of interest (not shown). The SYN1deg data set is used over the period 2000–2016 (Figure 1).

Following Miller et al. (2012), several parameters related to the radiative budget may be defined. One first defines the net radiation at the TOA as

$$R_{\text{net}}\left(\text{TOA}\right) = \text{rsdt} - \text{rlut} - \text{rsut} \tag{1}$$

where rsdt, rlut, and rsut are the incoming flux, the LW outgoing flux, and the SW outgoing flux at the TOA, respectively. Similarly, the net radiation budget at the surface reads

$$R_{\text{net}}\left(\text{BOA}\right) = \text{rsds} + \text{rlds} - \text{rsus} - \text{rlut} \tag{2}$$

where rsds and rlds are the SW and LW downwelling fluxes and rsus and rlus the SW and LW upwelling fluxes. The net column radiative divergence is then defined as

$$\text{Net Rad Div} = R_{\text{net}}\left(\text{TOA}\right) - R_{\text{net}}\left(\text{BOA}\right) \tag{3}$$

A positive Net Rad Div corresponds to a heating of the atmosphere by the radiation.

The modulation of the radiative budget by clouds can be investigated using the CERES SYN1deg data. The cloud radiative effects (CREs) at the TOA and at the surface (BOA) read

$$\begin{aligned}\text{CRE}\left(\text{TOA}\right) &= \text{rsut}_{\text{cs}} - \text{rsut} + \text{rlut}_{\text{cs}} - \text{rlut}\\ \text{CRE}\left(\text{BOA}\right) &= \text{rsds} - \text{rsds}_{\text{cs}} + \text{rlds} - \text{rlds}_{\text{cs}}\end{aligned} \tag{4}$$

where rsut_{cs} and rlut_{cs} are the SW and LW outgoing fluxes at the TOA, assuming clear-sky conditions and rsds_{cs} and rlds_{cs} are the SW and LW downwelling fluxes at the surface, also assuming clear-sky conditions. The clear-sky fluxes are obtained from cloud-free regions identified in the 1-km MODIS measurements (Loeb et al., 2018). The impact of clouds on the atmospheric system is estimated by computed the cloud radiative forcing (CRF) that can be expressed as follows:

$$\text{CRF} = \text{Net Rad Div} - \text{Net Rad Div}_{\text{cs}} \tag{5}$$

where $\text{Net Rad Div}_{\text{cs}}$ corresponds to the radiative flux divergence, assuming clear-sky conditions.

2.3. Precipitable Water, Cloud Properties, and Aerosol Optical Depth From MODIS Daily Data

Cloud, aerosol, and precipitable water are obtained from the MODIS instrument, onboard Terra and Aqua (King et al., 2003). Retrieval merging the measurements from the two instruments does not exist and the data sets derived from the two instruments are considered as independent samples (see Figure 1) with different lengths and sampling hours. MODIS observes TOA reflectance and radiance in 36 wavelength bands and provides daily data, which consist in statistics derived from level 2 atmospheric parameters. These products are aggregated onto a 1° × 1° global grid separately for each satellite.

The precipitable water (column water vapor amount, PW) is retrieved in the infrared (using day and nighttime measurements) and in the near infrared (during daytime) in clear-sky situations and above clouds. As we seek for measurements representative of daily averaged values, only the infrared product is considered below. PW is retrieved on an instantaneous basis from groups of 5 × 5 1-km pixels when at least nine pixels out of 25 are cloud free. King et al. (2003) compared the retrieved water vapor amounts with those measured using microwave radiometers, radiosondes, and GOES8 removing cloud contamination. They find that for dry atmospheres (lower than 17 mm), MODIS overestimates the precipitable water by 3 mm. In contrast, for wet cases (higher than 17 mm), MODIS is lower by 5.7 mm. This implies that MODIS retrieval reduces the magnitude of a PW gradient, even though MODIS still captures the small-scale structures of PW spatial gradients as well as their global changes from day to day (King et al., 2003).

Three different algorithms are separately implemented in order to retrieve aerosols properties from MODIS data depending on the surface characteristics. Here, we use the "Deep Blue" algorithm as it was specifically developed for bright surfaces (Hsu et al., 2004) and thus appears the best algorithm over the bare and sparsely vegetated soil of the Sahel in spring.

The Deep Blue retrieval is implemented for each single cloud-free pixel (at 1-km resolution near nadir and about 8-km resolution at edge) and then averaged in 10 × 10 pixels. The current Deep Blue algorithm considers a dynamic surface reflectance that depends on scattering angles and seasonal normalized differential vegetation index (Hsu et al., 2004) and on look-up tables of aerosol optical properties. As an output, it determines aerosol optical depth (AOD) and spectral single scattering albedos (ω) by matching computed apparent reflectance with satellite observed spectral radiances. The enhanced Deep Blue algorithm uses primarily satellite spectral radiances in the blue region (412 and 490 nm) but also ingests multiple bands between 412 nm and 12 μm to retrieve AOD and ω, simultaneously. The MODIS Collection 6 (C6), which implements the enhanced Deep Blue algorithm is used in the present study. The accuracy of satellite AOD estimates was first theoretically analyzed (Kaufman et al., 1997; Tanré et al., 1997), which yields a bias of ±0.03 over ocean and ±0.05 over land (mainly due to uncertainty in the estimate of surface reflectance). Tao et al. (2017) found a systematic underestimation for Deep Blue (C6) retrievals over all their sites located in desert regions of East Asia, especially during high AOD conditions. They also noted, in some regions such as the Taklimakan Desert, that MODIS Deep Blue AOD presents constant low values around 0.05 when AOD is below 0.5. For consistency with other data sets, the AOD estimated at 660 nm is considered here.

The MODIS product provides retrievals of cloud optical depth at 1-km resolution twice per day at 1330 and 0130 LT (Platnick et al., 2017). It is retrieved via look-up tables using SW reflectance measurements at one absorbing water wavelength and one nonabsorbing water wavelength.

2.4. Precipitable Water From AIRX3STD Data

The combination of the infrared spectrometer Atmospheric Infrared Sounder (AIRS) and the Advanced Microwave Sounding Unit (AMSU) onboard Aqua offers the advantage of measuring the radiation penetrating through clouds and polar darkness (Kang et al., 2005). The AIRS v6 retrieval algorithm now includes the use of a neural network trained to ECMWF model fields (Blackwell, 2005) to retrieve PW.

The AIRS Level 3 Daily Gridded Product contains standard retrieval means, standard deviations, and input counts for a temporal period of 24 h for either the descending (equatorial crossing North to South at 1:30 a.m. LT) or the ascending (equatorial crossing South to North at 1:30 p.m. LT) orbit. The geophysical parameters have been averaged and binned into 1° × 1° grid cells. For this study and due to the limited diurnal

variability of PW, ascending and descending data are averaged. Considering separately the two data sets has no impact on the results.

2.5. Aerosol Optical Depth From the Aerosol and Surface Albedo Retrieval Using a Directional Splitting Method-Application to Geostationary Daily Data

The AERUS-GEO (Aerosol and surface albEdo Retrieval Using a directional Splitting method-application to GEOstationary) data product is derived from observations of SEVIRI (Spinning Enhanced Visible and Infrared Imager) onboard the Meteosat Second Generation (MSG) geostationary satellite which acquires one full observation of the Earth's disk centered over Africa every 15 min. The spatial resolution of AERUS-GEO is about 4 km. By assuming that aerosol directional effects are more stationary than surface reflectance (time scale of several days), both signals are separated. The outputs delivered by the AERUS-GEO chain at a daily time scale, since 2005 (see Figure 1), are then the AOD at 0.63 μm and the Angstrom coefficient to determine the aerosol type. For the purpose of this study and for consistency with the other data sets, AOD are averaged on $1° \times 1°$ grid.

AOD retrievals from the AERUS-GEO have been widely evaluated. Carrer et al. (2010) validated the original method by comparing the AOD estimates to Aerosol Robotic Network (AERONET) ground observations and MODIS Collection 5 products. A mean bias lower than 20% was determined in comparison with AERONET measurements.

2.6. Heat Wave Identification and Physical Characterization

This study makes use of the HW index proposed by Barbier et al. (2018). HWs are defined as intraseasonal events whose signature can be found in either T_{max} (HW_{max}) or T_{min} (HW_{min}) daily temperature intraseasonal anomalies. First, at each location, a 90-day-high-pass filter is applied to temperature, then, the value of the ninetieth percentile of the temperature anomalies for the March–June period is determined. Each location/time for which either the T_{max} or the T_{min} anomaly exceeds this threshold is considered as an extreme temperature and is then grouped together. In order to focus on synoptic-scale events, a spatiotemporal constraint is applied to removes small size (less than 60 10^4 km^2) or short (under 3 days) events. Focusing on March–June, about 3 HW_{min} and HW_{max} events per year are obtained over a Sahelian domain (referred to as Sahel in the following) covering (10°N; 20°N) and (−10°E; 20°E) (see Barbier et al., 2018, for more details). We use the series of HW events obtained with this method. This separate detection of daytime and nighttime HW does not preclude that both occur simultaneously but only 20% of HW_{min} and HW_{max} occur simultaneously.

For each detected HW event, the spatially averaged values of physical parameters are computed within the Sahel region affected by the HW (solid lines in the example provided in Figure 2). Whatever its spatial extension, each day of a given event is then characterized by one unique value. However, only HW events for which at least 25% of its spatial extent is sampled by the spaceborne observations are kept for further analysis. As T_{min} is generally reached in the early morning, for any day of a HW_{min} event, we consider daily data from the previous day to compute its composite. Following Zhang et al. (2011), the daily observations are compared with the climatological value over the same area (Figure 2b) and an averaged anomaly value is computed for each documented HW. The climatological values are computed for each parameter and data set at each location within the Sahelian domain using the longest available record (see Figure 1) and a 9-day running mean window. The size of the smoothing window does not significantly impact the results. Note that it is difficult to strictly apply the 90-day-high-pass filter used in Barbier et al. (2018) to detect HW, due to the spatial and temporal discontinuities that exist in several observational data sets (as illustrated in Figure 2 for the MODIS sampling). A comparison of temperature anomalies computed using the climatology obtained using the high-pass filter or the mean and 9-day smoothing window is presented in Section 4. In the present work, HWs are characterized with anomalies that are computed with respect to the annual cycle.

Mean value of atmospheric parameters and corresponding anomalies are systematically computed for each HW event and each data set summarized in Table 1. Because of the various length of the data sets and their different ability in retrieving the atmospheric parameters, the number of days is not identical from

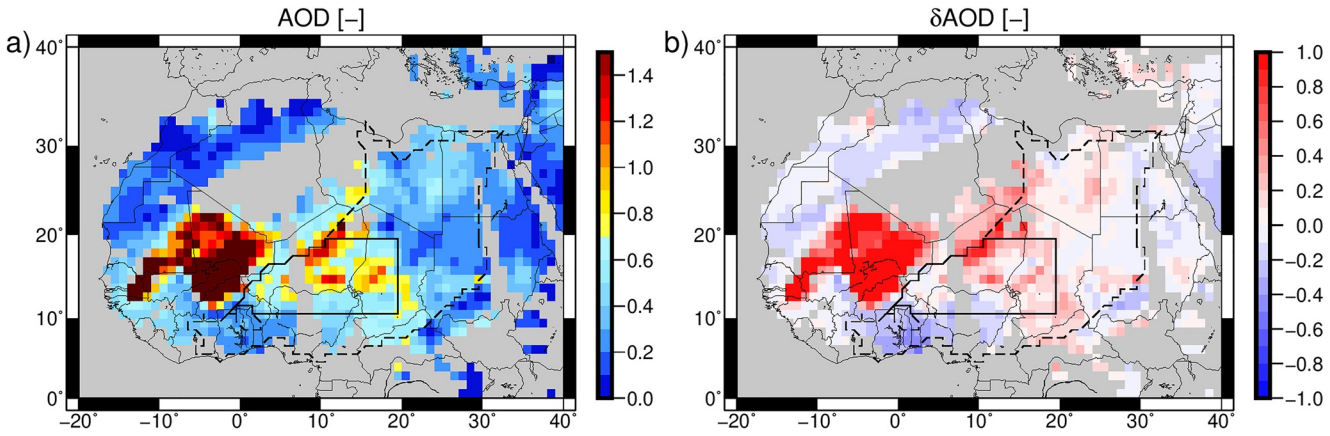

Figure 2. Illustration of the heat wave "characterization" process for the AOD at 660 nm derived from MODIS onboard Aqua on April 19, 2010, using the Deep Blue algorithm. (a) Raw AOD and (b) AOD anomalies with respect to their climatological annual cycle. The dashed line contours the heat wave event at the scale of Africa. The solid line delimited the part of the heat wave that affects the Sahel region as defined in the text and which is used to compute the mean value of AOD and the corresponding AOD anomaly of this event. AOD, aerosol optical depth; MODIS, Moderate Resolution Imaging Spectroradiometer.

one data set to the other and will systematically be indicated in the following analysis. For instance, BEST and CERES-SYN1deg data sets provide a continuous sampling at all points leading to identical numbers of documented days in HW for each atmospheric parameters, whereas MODIS has different number of days in HW among the various atmospheric parameters. Each inverted atmospheric parameter may be biased or affected by random error as detailed in the previous descriptions. However, we expect that the computation of averaged value reduces the random error and the computation of anomalies removes any systematic error (i.e., bias).

Distributions of mean values are computed from the daily HW samples and are shown in Section 4. To quantify, how the distribution of daily values in case of HW differs from the climatological values, the same distributions can be built for the climatological values extracted at the same time and place. Both distributions are then compared using a Kolmogorov–Smirnov test that quantifies the distance between the two distributions. If the associated *p*-value is small, it tells that the two populations have different distributions. The good continuity and duration of the BEST and CERES data sets ensure that covariations with other atmospheric parameters can be examined (see Section 5). This is done using Pearson's correlation coefficients. These correlation coefficient interpreted as significant when the associated *p*-value is smaller than 0.01.

3. Documenting the Mean Annual Cycle of the Sahel With Satellite Observations

Before analyzing the HW characteristics, we document the climatological characteristics of spring in the Sahel, as observed by satellites and ground observations. Figure 3 shows the spatiotemporal evolution of maximum and minimum temperature over West Africa using Hovmuller diagrams. For each day and latitude, data between (−10°E; 20°E) are averaged. Both T_{max} and T_{min} display a bimodal annual cycle over the Sahel with a maximum prior and after the monsoon season (T_{min} having a smoother behavior). The maximum value in T_{max} is reached later in the annual cycle as one moves to northern locations (from Day of Year 100 at 12°N to Day of Year 150 at 17°N). The occurrence of the highest T_{min} value is delayed by about 30 days compared to that of the highest T_{max} value. In this paper, the spring period corresponds to an enlarged spring (between Day of Year 60 [March 1] and 181 [June 30]) in order to largely cover the period where T_{min} and T_{max} are high. The latitudinal extend of the region of interest is shown by the black domain in Figure 3.

This hot period occurs before the annual maximum of PW over the Sahel (Figure 4), which is reached around mid-August (Day of Year 225), during the core of the monsoon season (Guichard et al., 2009; Slingo et al., 2009). The period prior to the monsoon corresponds to a gradual moistening between 10°N and 20°N (Couvreux et al., 2010). The PW at the northern edge of the domain never exceeds 30 mm and can drop down to 10 mm at the beginning of the considered period. Some differences exist among Terra and Aqua

Table 1
Number of Days in HW Events for Each Atmospheric Parameter of Each Data Sets for Which a Mean Value (and Corresponding Anomaly With Respect to the Climatology) Can Be Computed

Data set	Atmospheric parameter	Number of HW_{min} days	Number of HW_{max} days
BEST	T_{min}	845	909
	T_{max}	845	909
	T_{mean}	845	909
CERES SYN1deg	rsds	164	191
	rlds	164	191
MODIS Aqua	AOD	130	156
	PW	131	157
	COT	122	105
MODIS Terra	AOD	164	191
	PW	164	191
	COT	142	112
AERUS-GEO	AOD	99	129
AIRX3STD	PW	128	157

(Figures 4a and 4b), with Aqua data having larger values of PW by about 1–1.5 mm over most of the domain and even 2 mm for the wettest values. The difference can exceed 5 mm during the monsoon, especially between 5°N and 10°N. This behavior is not linked to the different time span of the two data sets, since using only the Aqua period to compute the Terra climatology leads to similar results (not shown). One may also argue that both satellites do not have similar equator crossing time, 10:30 LT and 13:30 LT for Terra and Aqua, respectively, and that this difference may be linked to the diurnal cycle. Such a difference appears however much larger than indicated by GPS data over the Sahel (e.g., Bock et al., 2008; Figure 11). Furthermore, the AIRX3STD PW estimates (Figure 4c) retrieved from AIRS and AMSU also onboard Aqua are closer to the Terra estimates (Figure 4a). A possible explanation may be sought in the MODIS retrieval algorithm and in the cloud diurnal cycle. As explained in Section 2.3, PW is computed from cloud-free pixels. Hill et al. (2016) studied the cloud diurnal cycle over Southern West Africa using different cloud products and note that the cloud detection by passive instruments may be affected in case of multiple cloud layers. One can assume that the differences between both MODIS data sets are the results of cloud misdetection within the diurnal cycle, thus explaining why the disagreement is larger in the southern part of the domain or during the core of the monsoon season. However, this hypothesis deserves more investigations that are beyond the scope of this paper.

The three AOD estimates consistently indicate that the spring period is also associated with the largest annual AOD (higher than 0.5, Figure 5), as already documented with ground-based observations in Marticorena et al. (2010) and Slingo et al. (2009). The maximum AOD shifts northward after the occurrence of the first convective systems in the Sahel (around Day of Year 150). Some differences between the three AOD products are worthwhile mentioning. If a background value of AOD close to 0.5 is found in the Sahel, both MODIS estimates (Figures 5a and 5b) show similar values and fluctuations which can be up to 0.8 (this value may even be underestimated according to Tao et al. [2017] who found using instantaneous comparisons with MODIS and MISR that the Deep Blue C6 product is lower by about 0.05). In contrast, the AERUS-GEO product (Figure 5c) does not capture AOD much higher than this background value. Carrer et al. (2010) note a potential 20% underestimation with respect to AERONET measurements.

Net radiation fluxes given by Equations 1 and 2 are shown in Figures 6a and 6b, respectively. At TOA, the net radiative budget has positive values over the southern part of the Sahel domain with maximum values reached during spring. Positive values mean that the Earth–Atmosphere system is gaining energy from

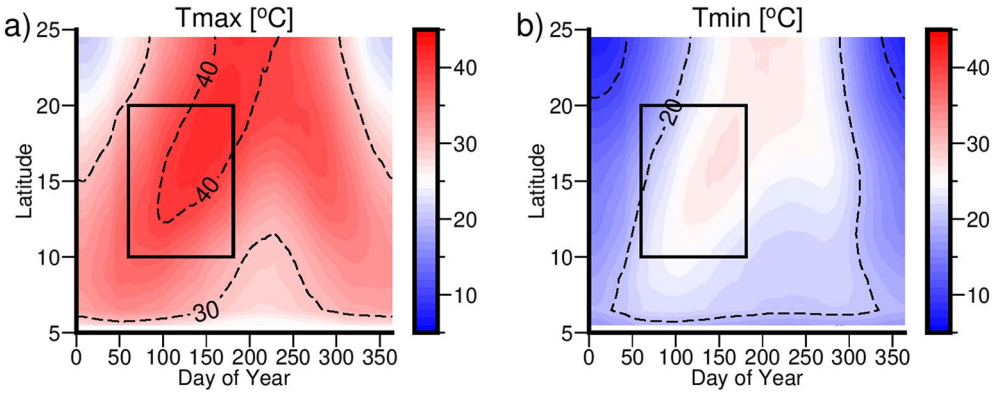

Figure 3. Hovmuller diagram over West Africa of the annual cycle of the BEST (a) maximum temperature and (b) minimum temperature, averaged over the band (−10°E; 20°E) (in °C). The spatiotemporal domain in which HWs are studied is highlighted by the black rectangle. BEST, Berkeley Earth Surface Temperature; HW, heat wave.

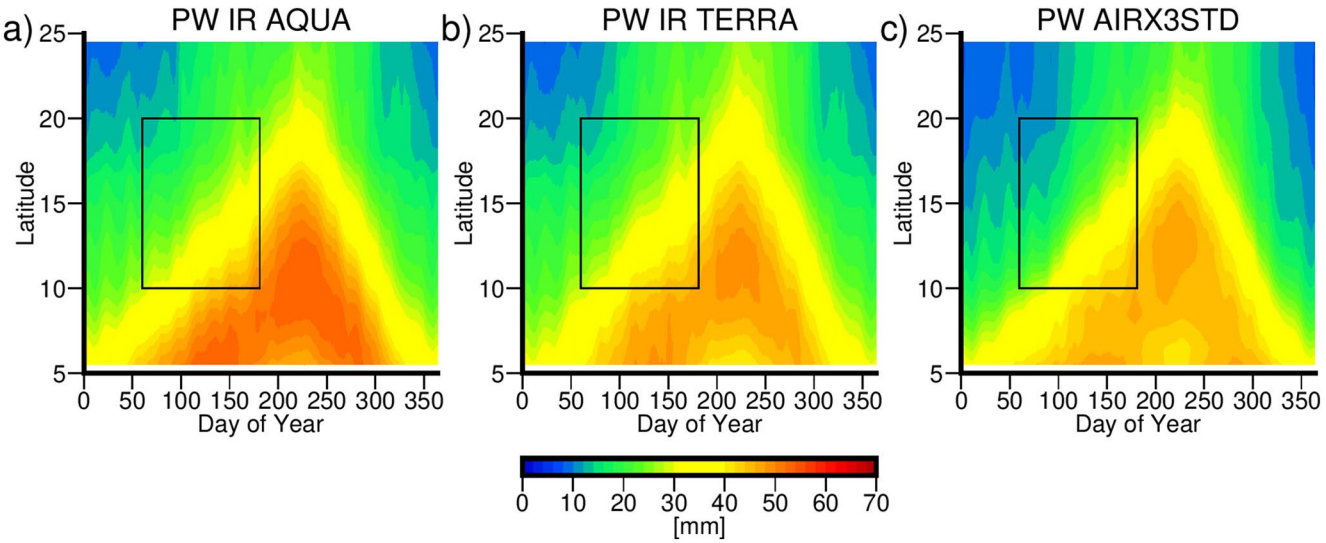

Figure 4. Hovmuller diagrams of the PW annual cycle averaged over (−10°E; 20°E) over West Africa from (a) MODIS on Aqua, (b) MODIS on Terra, and (c) AIRX3STD (in mm). The black box corresponds to the latitudinal and temporal boundaries considered in the present study. PW, precipitable water; MODIS, Moderate Resolution Imaging Spectroradiometer.

radiation. The northern part of the domain looses energy at the beginning of the period and reaches small positive values by the beginning of April (Day of Year 100). At BOA, R_{net} is positive, implying that the surface is also gaining energy with a larger magnitude in the southern part of the domain.

The net column radiative divergence is shown in Figure 6c. In the present case, this parameter is negative with values even smaller than the smallest R_{net} at TOA (in particular up to Day of Year 100 in the northernmost part of the Sahel domain). It means that the surface is gaining energy at the expense of the atmosphere with a rate varying between 50 and 80 W m^{-2}. This estimate is consistent with the 75 W m^{-2} found by Slingo et al. (2009) at Niamey.

Figures 6d and 6e show CRE at TOA and BOA, respectively (see Equation 4). At the TOA, CRE is positive (up to 40 W m^{-2} near 12°N) over most of the domain. These positive values indicate that the clouds warm

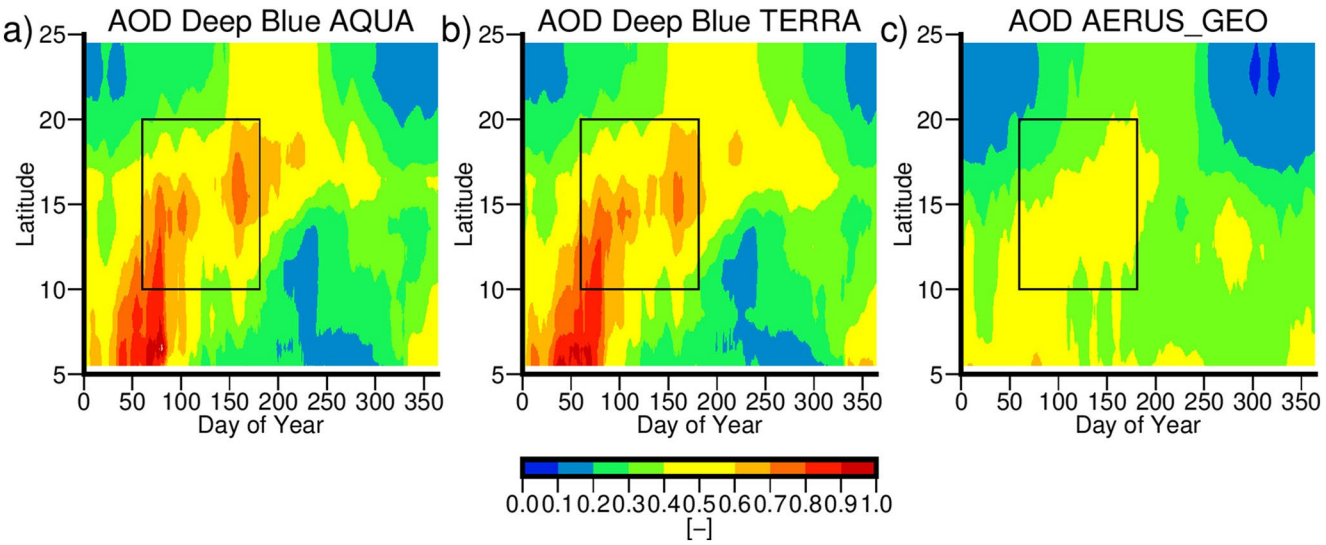

Figure 5. Hovmuller diagram of the 660-nm AOD annual cycle averaged over (−10°E; 20°E) (a) from Deep Blue retrieval applied to MODIS on Aqua, (b) from Deep Blue retrieval applied on MODIS on Terra, and (c) from AERUS-GEO. AOD, aerosol optical depth; MODIS, Moderate Resolution Imaging Spectroradiometer; AERUS-GEO, Aerosol and surface albEdo Retrieval Using a directional Splitting method-application to GEOstationary.

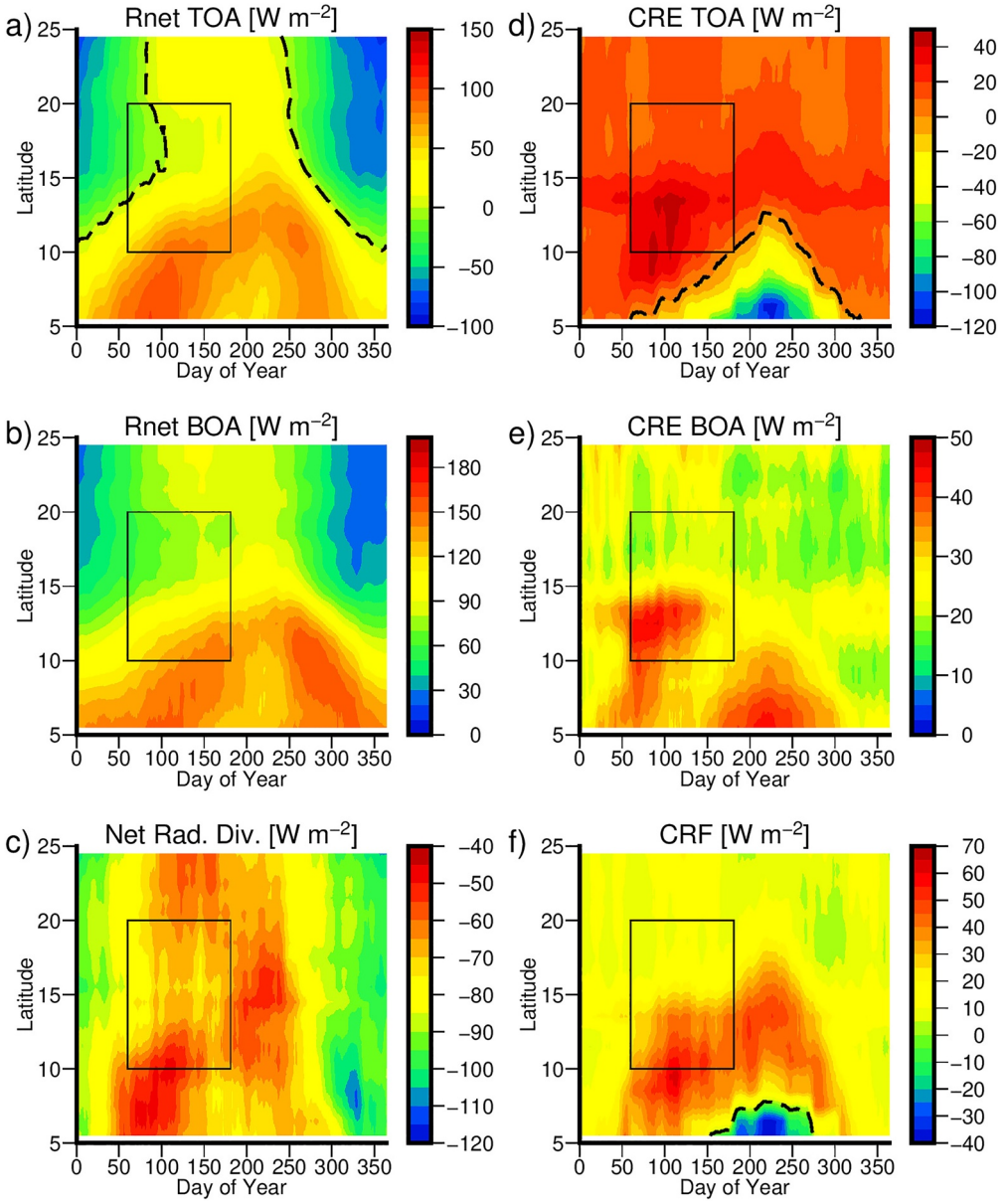

Figure 6. Hovmuller diagram of the annual cycle of the CERES SYN1deg (a) net radiation balance at the TOA, (b) net radiation balance at the surface, (c) atmospheric radiative flux divergence, (d) cloud radiative effect at TOA, (e) cloud radiative effect at the surface, and (f) cloud radiative forcing, averaged over (−10°E; 20°E) (in W m^{-2}). The dashed line shows the 0 W m^{-2} level. CERES, Clouds and the Earth's Radiant Energy System; TOA, Top Of the Atmosphere.

the atmosphere–surface system and result from a domination of the cloud effect in the LW (not shown). The LW cloud effect also dominates at the surface with a positive CRE that can reaches 40 W m^{-2}, especially between April and June in the southern part of the domain. This indicates that clouds provide an excess of energy to the surface.

The impact of clouds on the atmospheric system is measured by the CRF (Equation 5 and Figure 6f), which is positive over the whole domain (up to 50 W m^{-2} in the southern part of the domain for the spring period): clouds thus warm the atmosphere and reduce its loss of energy. The potential role of clouds in the occurrence of highest atmospheric temperatures during spring will be investigated hereafter.

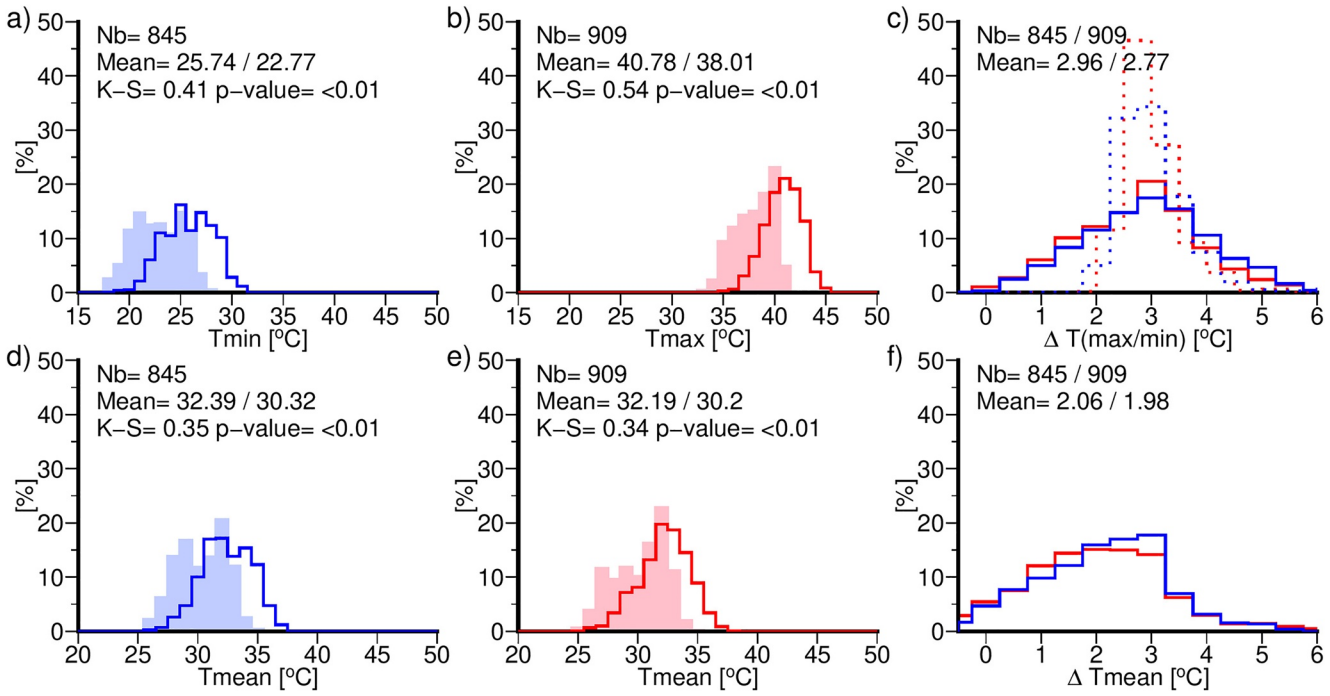

Figure 7. Distribution of (a) T_{min} for HW_{min} and (b) T_{max} for HW_{max} events in °C superimposed to the distribution of the respective climatological values in filled histograms and (c) the corresponding anomalies. Dotted lines show the anomalies using the high-pass filter of Barbier et al. (2018). (d–f) Identical to (a)–(c) but for mean daily temperature. Numbers at the top left of each panel show the number of days in HW_{min}/HW_{max} events considered in the distributions, the corresponding mean value is also shown, with first the mean value in HW events and the mean value of the climatology. For (a) ,(b), (d), and (e), the result of the Kolmogorov–Smirnov test is also shown. HW, heat wave.

4. Mean Heat Wave Characteristics

The objective of this section is to document several atmospheric parameters during HW events and to assess possible departures from their climatological values. For each HW event, an average value over the selected region (HW region intersecting the Sahel domain considered here) is computed for each individual physical parameter as well as an average of its anomaly. Their distributions among the HW_{max} and HW_{min} events are then examined.

First, we compare the magnitude of temperature anomalies derived from the detection method of Barbier et al. (2018) and from our method (using a 9-day running mean). Figure 7 shows the distribution of mean T_{max} during HW_{max} events and that of mean T_{min} during HW_{min} events, as well as the distribution of their corresponding anomalies either with respect to the BEST climatology shown in Figure 3 (solid lines) or with respect to the high-pass filter of Barbier et al. (2018) (dotted lines). The mean anomaly distributions found when using the high-pass filter are narrower compared with the ones obtained from the 9-day running mean. In both HW types, the temperature anomalies have similar mean values: 2.96°C and 2.77°C in case of HW_{min} and HW_{max} compared to 3°C for both types of event. HW_{max} events correspond to a mean T_{max} value of 40°C, which can reach 45°C. During HW_{min} events, the mean T_{min} value is around 25°C but values as high as 30°C can also occur. The distributions of T_{min}/T_{max} obtained in case of HW significantly differ from the distribution of climatological values as indicated by the results of the Kolmogorov–Smirnov test.

Measurements of these extreme daily temperatures correspond to instantaneous temperatures. It is then of interest to examine the distribution of T_{mean} (shown in Figures 7d and 7e). Very similar distributions are obtained for both types of events with an average T_{mean} of 32°C, 2°C higher than the climatology. This suggests compensation between night and day time temperature with a reduced diurnal temperature range (DTR) in case of HW_{min} events and an increased DTR in case of HW_{max} events, consistently with Barbier et al. (2018).

Intuitively, one may assume that atmospheric processes tend to amplify the temperature near the surface through an increase of surface incoming radiative fluxes. Indeed, the total incoming fluxes are, on average,

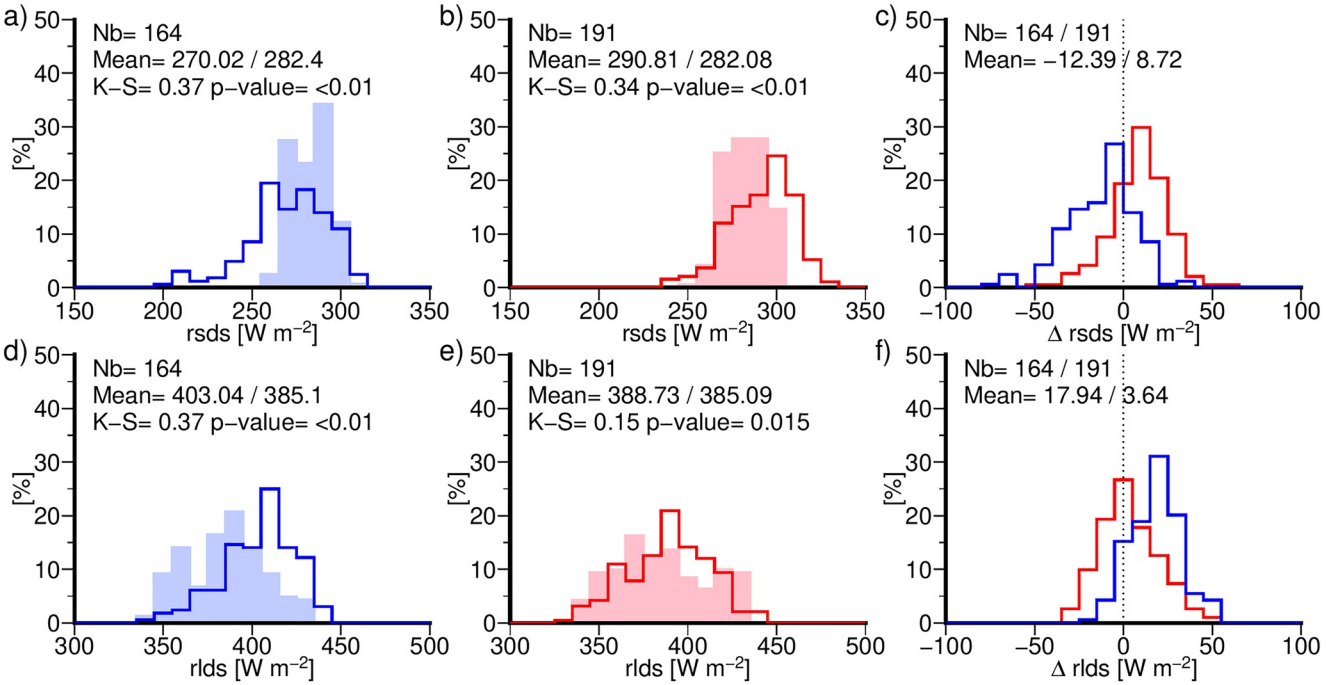

Figure 8. Distribution of incoming (a, b) SW and (d, e) LW fluxes at the surface (a, d) for HW_{min} (blue) and (b, e) HW_{max} (red) events (solid line) and for the climatology (filled) derived from CERES SYN1deg Ed4A daily. Numbers at the top left of each panel show the number of HW considered in the distributions; the corresponding mean value is also shown for HW and for the climatology. The results of a Kolmogorov–Smirnov (K–S) test between the two distributions are also given. (c, f) Distribution of the anomalies with respect to the climatology. Number of HW_{min}/HW_{max} and mean value of anomalies for HW_{min}/HW_{max} are also shown. SW, shortwave; LW, longwave; CERES, Clouds and the Earth's Radiant Energy System; HW, heat wave.

increased by 5.5 and 12.3 W m^{-2} with respect to climatology during HW_{min} and HW_{max} events, respectively (not shown). The contribution of the SW and LW incoming fluxes at the surface (rsds and rlds) is nevertheless distinct between the two types of HW (Figure 8). Smaller values of rsds are found in case of HW_{min} events than in HW_{max} events corresponding to a negative anomaly for HW_{min} events and to a positive anomaly for HW_{max} events, both distributions being significantly different from the climatological distributions. Two major sources may explain the HW_{min} results in the SW domain, namely an increase in the AOD or a larger CRE. These potential contributions are investigated in Section 5. This negative anomaly is balanced in the LW by large positive anomaly observed in case of HW_{min} events (Figure 8f). The picture is more complex during HW_{max} events, with more centered distributions, not significantly different from climatological distributions. Several effects may contribute to a LW anomaly: water vapor, aerosol, and clouds. Note that the small anomaly in total incoming fluxes in case of HW_{min} events results of a compensating effect between the SW and LW fluxes, while in case of HW_{max} both flux anomalies are adding up.

Surface LW emission may also contribute to an increase of the near-surface temperature. Reinforcement of LW emission may have several origins. For instance, accumulation of sensible heat by absorption of solar energy during the days preceding the HW as suggested by Seluchi et al. (2006) or a more direct response of the ground surface in case of HW where abnormally hot temperature would result in a positive anomaly of upcoming LW flux. CERES SYN1deg data set provides also estimates of the upwelling fluxes with mean anomalies of 6.5 W m^{-2} in case of HW_{min} and 11.3 W m^{-2} in case of HW_{max} (not shown). These positive anomalies nearly balance with the anomalies in incoming fluxes suggesting an instantaneous response of the surface rather than a delayed effect of previous day heat accumulation.

The distributions of the AOD at 660 nm obtained from the three available spaceborne retrievals (see Section 2) are shown in Figure 9. The two MODIS Deep Blue AOD products obtained from the Terra or the Aqua satellites give rather similar shape of the AOD distributions (Figures 9a, 9b, 9d, and 9e). However, consistently with the climatologies shown in Figure 5, MODIS distributions are slightly shifted toward higher values, compared to the AERUS product (Figures 9g and 9h). The AERUS AOD estimates are on

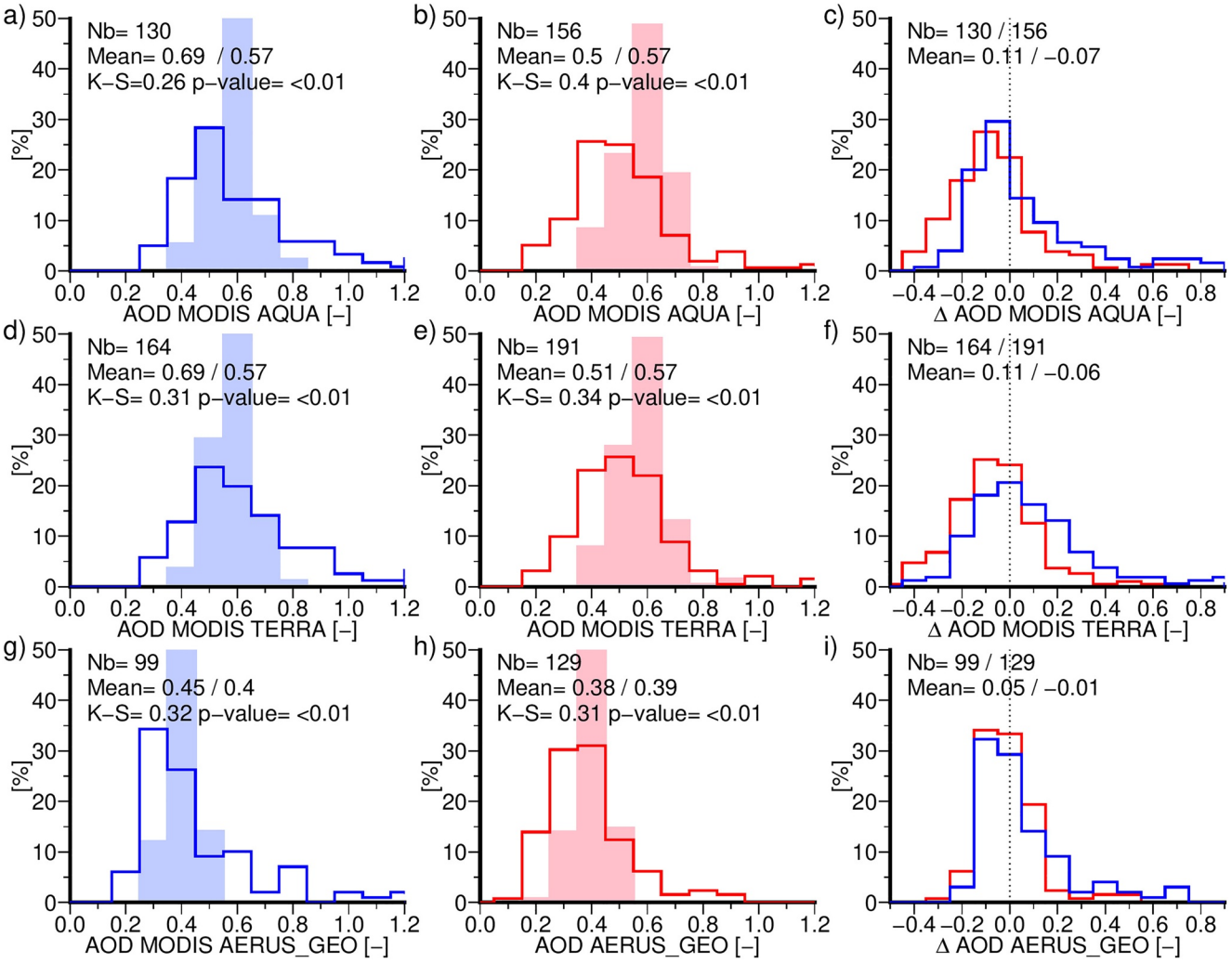

Figure 9. Same as Figure 8 but for retrieved aerosol optical depth at 660 nm from MODIS on Aqua (a–c), MODIS on Terra (d–f), and AERUS-GEO product (g–i). MODIS, Moderate Resolution Imaging Spectroradiometer; AERUS-GEO, Aerosol and surface albEdo Retrieval Using a directional Splitting method-application to GEOstationary.

average about 0.15 smaller. This value exceeds the biases documented in Carrer et al. (2010) with respect to AERONET measurements. However, for all products and both types of HW, the distribution is wider and shows significant departure from the climatology in case of HW.

Whatever the retrieval, the averaged AOD anomalies behave similarly in case of HW events: HW_{min} events correspond to a positive (0.1) AOD anomaly while during HW_{max} events, AOD anomalies are slightly negative. The HW_{min} distribution has a positive skewness (exceeding 1.5 for all data sets), with AOD anomalies that can reach values higher than 0.4. The positive mean anomaly results then from numerous situations where the AOD is close or slightly less than its climatological value. An averaged anomaly of −0.10, mixing all data sets, is found for HW_{min} with negative AOD anomalies with respect to an anomaly of 0.28 for those having a positive anomaly. This result suggests that AOD radiative effect may be involved in about half of HW_{min} events. This increase in aerosol may contribute to the reduction of rsds for some HW_{min}.

The distribution of anomalies is also positively skewed for HW_{max} with skewness values of 1.27, 0.77, and 1.77 for MODIS Aqua, MODIS Terra, and AERUS, respectively. Positive anomalies are observed in about one third of HW_{max} cases and have a mean value of 0.13. The other two thirds of HW_{max} have a negative anomaly of −0.13. The positive skewness in this case is then the results of individual HW_{max} events with abnormally high AOD but a majority of events have rather a lower than usual atmospheric load in aerosols.

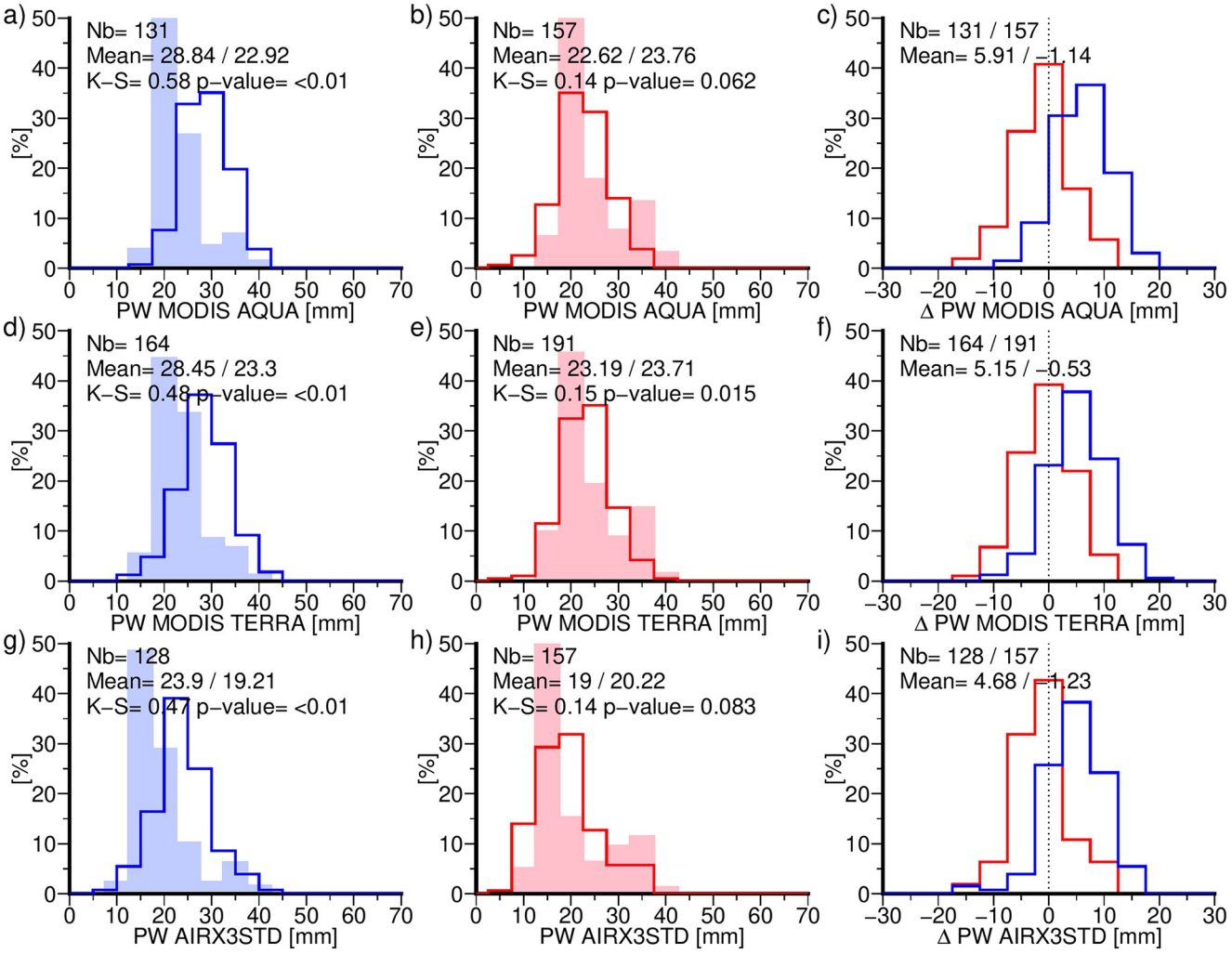

Figure 10. Same as Figure 8 but for PW retrieved from MODIS (infrared daily product) on Aqua (a–c), MODIS (infrared daily product) on Terra (d–f), and AIRX3STD product (g–i). PW, precipitable water; MODIS, Moderate Resolution Imaging Spectroradiometer.

The other parameter that may influence the incoming surface fluxes in clear-sky conditions, in particular in the LW domain, is the amount of humidity present in the atmosphere. This amount is quantified through the PW distribution shown in Figure 10. Independently of the product, the mean PW is slightly higher (about 5 mm) for HW_{min} events than for HW_{max} events. The AIRX3STD product (Figures 10g and 10h) systematically shows lower values compared to both MODIS retrievals (Figures 10a, 10b, 10d, and 10e. One may also note that the higher values of PW are obtained for HWs occurring after the month of April in agreement with the seasonal evolution (Figure 4). Maximum temperatures for these events do not exceed 42°C–43°C. This seasonal signal does not exist when anomalies are considered. Distributions of PW in case of HW_{max} do not significantly depart from the climatology (Figures 10b, 10e, and 10h, leading to small negative anomalies.

The values found in case of HW_{min} correspond to a positive PW anomaly of about 5 mm with respect to the climatology. Note that working with anomalies remove the contribution due to the systematic differences observed among data sets (see Figure 4). This increase in PW can contribute to the positive anomaly found in rlds in case of HW_{min} and with a smaller order of magnitude to the reduction of the rsds.

Cloud occurrence has a direct effect on surface fluxes. The CERES SYN1Deg product provides an estimation of the SW and LW CRE at the surface (Section 2.2). The HW_{min} and HW_{max} distributions are shown in Figure 11 together with that of the cloud optical thickness deduced from the MODIS instruments onboard

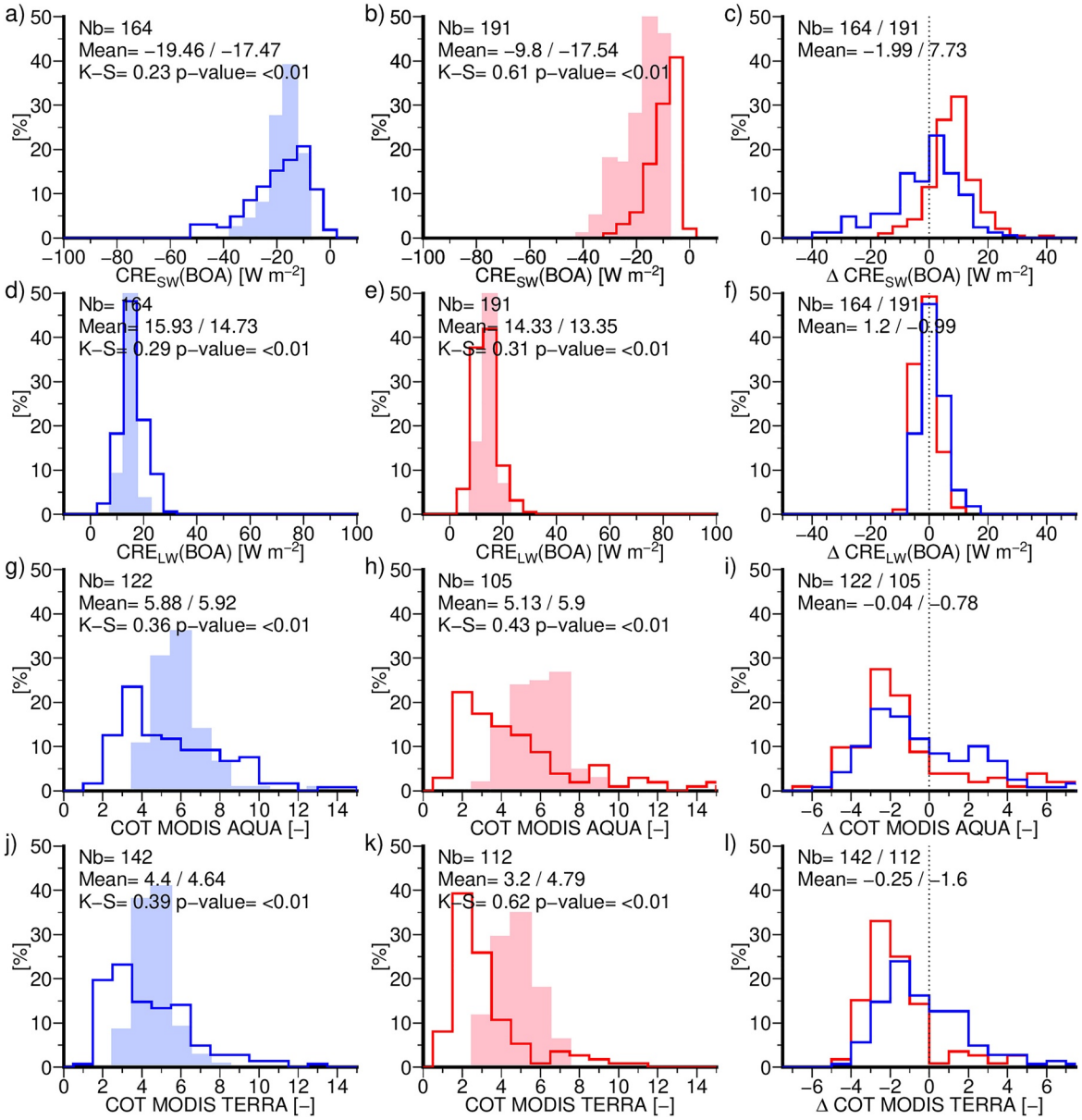

Figure 11. Same as Figure 8 but for cloud radiative effect in the SW at the surface (a–c) and in the LW at the surface (d–f) retrieved from CERES daily product and Cloud Optical thickness retrieved from MODIS onboard Aqua (g–i) and Terra (j–l). SW, shortwave; LW, longwave; CERES, Clouds and the Earth's Radiant Energy System; MODIS, Moderate Resolution Imaging Spectroradiometer.

Aqua and Terra. Clouds have more effect in the SW in case of HW_{min} (−19.46 W m^{-2}) than in HW_{max} events (−9.80 W m^{-2}) suggesting a role of clouds in the decrease in the rsds in the case of HW_{min}. Such situations are effectively affected by a negative anomaly of CRE. This anomaly is however the result of compensating effects between all-sky and clear-sky incoming fluxes. Indeed the CRE anomaly in the SW (noted ΔCRE_{SW}) reads

$$\begin{aligned} \Delta CRE_{SW} &= \Delta rsds - \Delta rsds_{cs} \\ \Delta CRE_{LW} &= \Delta rlds - \Delta rlds_{cs} \end{aligned} \quad (6)$$

As shown by Figure 8b, the HW_{min} anomaly in incoming flux is −12.39 W m^{-2}. It means therefore that more than 80% of the change in the incoming SW flux is due to the change in the clear-sky radiation, in particular

because of the higher atmospheric aerosol loading. This partition is supported by the weak anomalies observed in COT in spite of a significantly different distribution in case of HW_{min}.

One observes the opposite situations in case of HW_{max}, with a positive ΔCRE_{SW} mainly resulting from an increase in incoming SW fluxes (7.73 W m^{-2}) where the clear-sky variation explains about 10% of the change. A decrease in the cloud optical thickness is observed in case of HW_{max} and explains this positive anomaly as shown in Figures 11h, 11i, 11k, and 11l.

The CRE_{LW} anomaly is slightly positive for HW_{min} cases, but as for the SW, more than 90% of the anomaly is explained by the anomaly in clear-sky radiation due to the water vapor and aerosol contributions. For HW_{max}, the changes in clear-sky radiation explain the change in incoming LW fluxes but no direct signature is found in aerosol or water vapor.

As a summary, HW_{min} and HW_{max} events have similar properties in daily mean temperature but the separate process analysis of both HW points toward different effects explaining the observed heat excess. HW_{min} events are generally associated with an increased radiative effect of water vapor and in some occasion with a higher aerosol atmospheric loading. Both effects lead to a relatively neutral situation in term of net incoming fluxes at the surface. HW_{max} events are associated with an increase of incoming fluxes mainly resulting from processes in the SW domains that are likely related to a decrease in the cloud optical thickness and a moderate decrease of the aerosol loading in the atmosphere.

5. Radiative Budgets During Heat Wave Events

Several candidates for the increase of the atmospheric temperature associated with HWs have been identified in the previous section. We now investigate possible causal relationships through the search of covariations of these various parameters as well as possible subcategories among HW_{min} and HW_{max} events. A quantitative assessment of the role of the different atmospheric factors on the thermodynamic profile is beyond the scope of the present work, as it would require the use of a radiative transfer model. Such an approach needs a careful consideration on cloud and aerosol layering and radiative properties which may change from one day to the other. This is a complex task in a climatological approach.

The role of incoming fluxes at the surface in HW is further explored in Figure 12, by considering the relationship between incoming surface flux anomalies and T_{min} and T_{max} anomalies. The corresponding Pearson's correlation coefficients and associated p-values are shown in Table 2. This table also includes the correlations with the daily mean temperature. One basically observes an increase in T_{min} and T_{max} when the incoming fluxes (R_{in}) increase in case of HW_{min} and HW_{max}, respectively. T_{mean} correlates also well with this parameter showing the response of temperature to incoming fluxes. High correlation is expected between temperature and R_{in} (Guichard et al., 2009), mainly in response to the rsds annual cycle. However, in case of HW_{min}, the picture appears a bit different with high correlations resulting mainly from processes in the LW domain especially (correlation of 0.84). Spring is also the period where the higher fluctuations in PW are observed (Couvreux et al., 2010) that may explain this large contribution of rlds and this will be further investigated in the following. The picture is more complex for HW_{max} events, where no particular correlation is found with rlds or rsds. For both types of events, T_{mean} in these cases being highly correlated with rlds.

Correlations between temperature anomalies and R_{in} anomalies remain weak for both HW types, mainly because of compensating relationships in the LW and in the SW domains. This suggests therefore that the HW temperature increase emerges from complex interactions between the various radiative processes. Nevertheless temperature increases are generally associated with positive rlds anomalies (relatively high correlation for both HW types—Table 2), while they are anticorrelated with rsds anomalies. Beyond these quantitative correlation coefficients, it is also of interest to analyze the respective signs of anomalies. Figure 12 includes for each parameter the fraction of HWs with positive and negative anomalies of a particular field. Ninety-three percent of HW_{max} events are associated with positive anomalies of R_{in} and 75% of them correspond to positive anomalies of rsds. Among these events, more than one half has a positive anomaly of rlds. One observes that the lower anomalies in T_{max} (under 3 K) mainly correspond to positive anomalies in rsds and to negative rlds anomalies suggesting a cleaner and drier atmosphere.

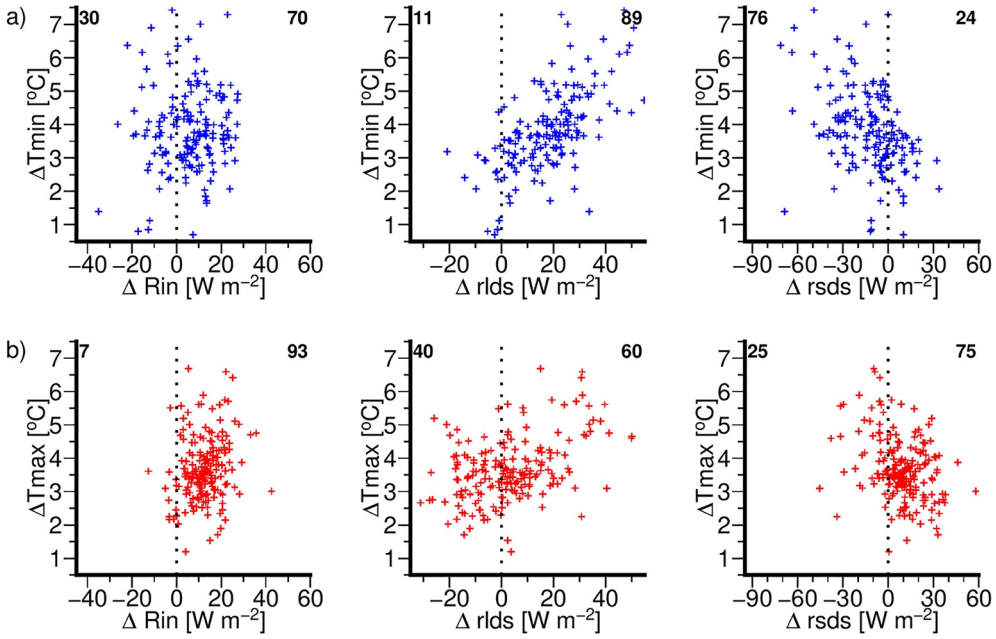

Figure 12. Scatter plot of (a) anomalies in T_{min} in case of HW_{min} and (b) anomalies in T_{max} in case of HW_{max} as a function of anomalies in R_{in}, rlds, and rsds. Numbers at the top left and right corners indicate the fraction (in %) of HWs with negative (left corner) and positive (right corner) anomalies. HW, heat wave.

Concerning HW_{min} events, only two thirds of them have a positive anomaly in R_{in}, even though 89% of them exhibit a positive anomaly in rlds and a high correlation coefficient. A large fraction of HW_{min} events associated with a negative anomaly in rsds (reduced incoming flux), with the largest negative anomalies in rsds corresponding to the largest anomalies in T_{min}. Such a combination tends to reduce the DTR by reducing T_{max}. The present analysis thus highlights different behaviors among each HW types, suggesting that the introduction of HW subcategories may be relevant to better understand the processes at play.

The relationships between various atmospheric parameters (surface radiative fluxes, COT, AOD, and PW) are then examined. Some expected covariances are obtained, whatever the HW type: an increase in PW leads to an increases in rlds through the water vapor greenhouse effect (not shown). This behavior was expected from the Prata (1996) formula, which states that for a given temperature, a moister atmosphere increases the atmospheric emissivity. This process was shown to be an important mechanism in case of nocturnal HW

Table 2
Pearson's Correlation Coefficients and Corresponding p-Values Between T_{min}, T_{max}, T_{mean}, and Incoming Radiative Fluxes at the Surface (and Their Anomalies) for Both HW_{max} and HW_{min} Events

Correlation/*p*-value		R_{in}	rlds	rsds
HW_{min}	T_{min}	0.74/<0.01	0.85/<0.01	$0.15/1.19 \times 10^{-1}$
	T_{mean}	0.80/<0.01	0.72/<0.01	0.34/<0.01
HW_{max}	T_{max}	0.69/<0.01	0.47/<0.01	0.47/<0.01
	T_{mean}	0.81/<0.01	0.81/<0.01	0.21/<0.01
Correlation/*p*-value		ΔR_{in}	Δrlds	Δrsds
HW_{min}	ΔT_{min}	$-0.080/7.97 \times 10^{-1}$	0.63/<0.01	−0.41/<0.01
	ΔT_{mean}	0.37/<0.01	0.38/<0.01	$-0.045/2.24 \times 10^{-1}$
HW_{max}	ΔT_{max}	0.24/<0.01	0.41/<0.01	−0.29/<0.01
	ΔT_{mean}	0.31/<0.01	0.70/<0.01	−0.55/<0.01

Note. Correlations, which are not significant at the 1% level are shaded.

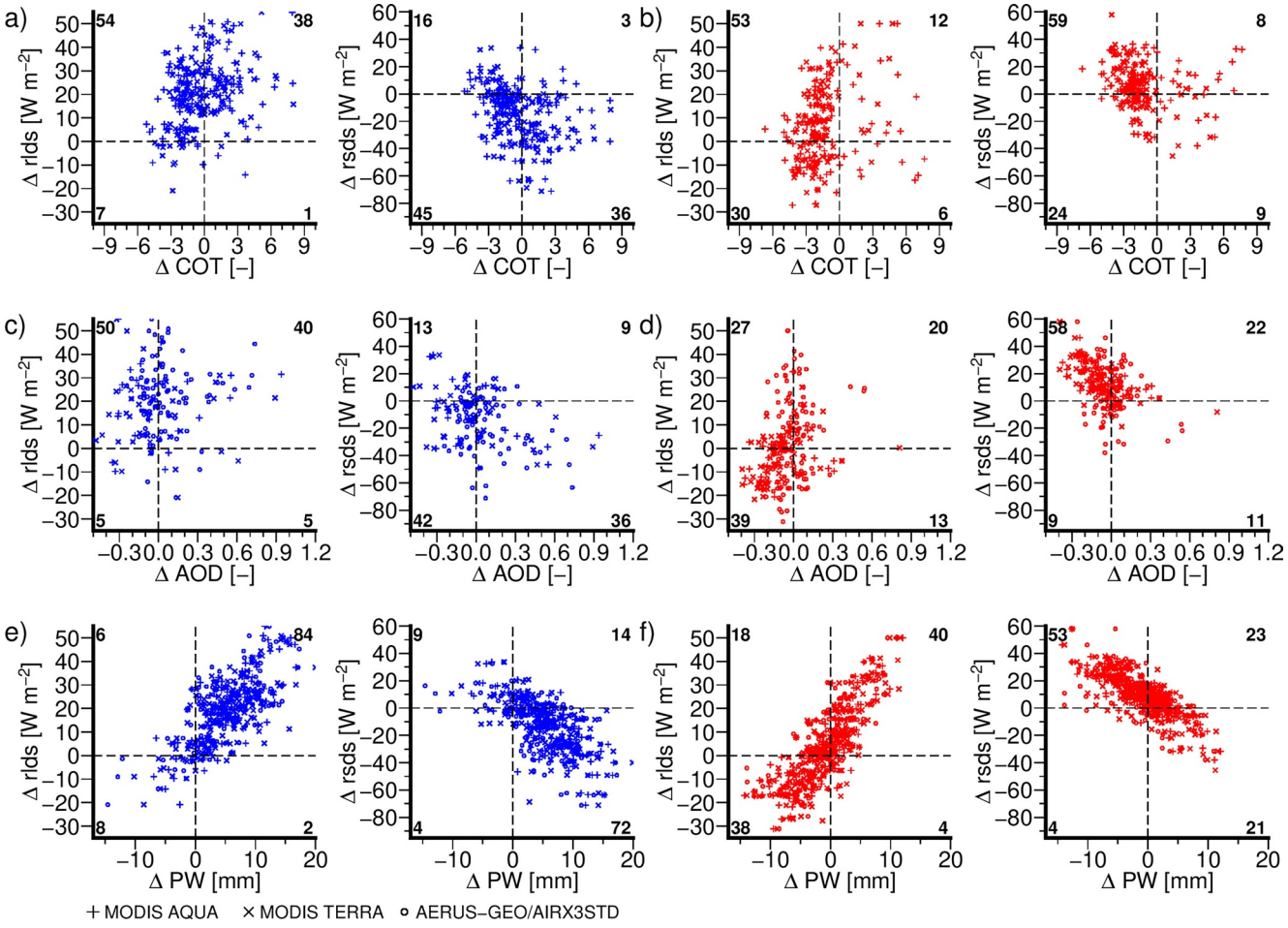

Figure 13. Scatter plot of anomalies in incoming fluxes at the surface as a function of anomalies in Cloud Optical Thickness (a, b), AOD (c, d), and PW (e, f) in case of HW_{min} (a, c, e) and HW_{max} (b, d, e) events. Each symbol corresponds to a different data set. Numbers at the at each panel corners indicate the fraction (in %) of heat waves in the corresponding quarter. AOD, aerosol optical depth; PW, precipitable water.

in Largeron et al. (2020). Similarly, a higher aerosol loading reduces rsds (not shown). Figure 13 documents the relationships between atmospheric parameter anomalies during HW_{max} (a, c, and e) and HW_{min} (b, d, and f) events, using all the available data sets analyzed in Section 3. As we are working with anomalies, the systematic biases of each data set are removed and the results are rather consistent, and thus robust. Note also that a multivariate statistical analysis is not yet possible because, in a wide majority of HW events, all the atmospheric control variables are not always available. In case of HW_{max} events, the majority of positive SW anomalies is well explained by a substantial decrease in COT (58% of the HW_{max} events located in the upper left corner). Negative anomalies of AOD and PW associated with an increase in rsds are also found for more than half of the HW_{max} cases (57% and 54%, respectively). Therefore, HW_{max} events seem to be associated with clearer and cleaner atmosphere compared to the climatology. This configuration allows the surface to cool more efficiently out to space during nighttime (Slingo et al., 2009) and therefore increases the DTR. As in Figure 12, the relationships appear complex in the LW domain, except for PW, with no systematic behavior. The more intense HW_{max} (larger anomalies in T_{max}) corresponds to negative anomalies in rsds which corresponds to in general a weak anomaly either in COT or AOD but a positive anomaly in PW that increases rlds. This process will then limit T_{min} and the corresponding DTR, leading then to the definition of a subcategory within the HW_{max}: limitation of the atmosphere transparency but a reinforcement of the heat through processes in the LW domain.

Concerning HW_{min} events, the main signature is found for PW with a wide majority of the events showing simultaneously a positive anomaly of rlds (89%) and a negative anomaly of rsds (76%). Even if one can argue

that an increase in PW can decrease the atmospheric SW transmittance, this effect should remain limited. In any case, one half of the HW_{min} situations are associated with an increase in AOD (the other half corresponding to relatively small negative anomalies), thus consistent with a weakening of the incoming SW radiation at the surface. The more intense HW_{min} are associated with the larger negative anomalies in rsds which corresponds to the higher positive AOD anomalies. Positive anomalies in AOD can also contribute to the positive anomalies in the LW domain by trapping and emitting LW radiation in particular during nighttime (Mallet et al., 2009). The HW_{min} limitation of rsds and the strengthening of the rlds tend then to decrease the DTR, as found by Barbier et al. (2018).

6. Conclusions

The present study aims at documenting the atmospheric processes that can contribute to an increase of near-surface temperature during HWs over the Sahel in spring. We focus on the role of the radiation budget at the surface and therefore analyze also the variables that control this radiative budget (precipitable water, AOD, clouds). Since the studied HW events correspond to synoptic-scale events, spaceborne observations, in particular because of their wide swath, are particularly suited for this documentation. However, geophysical parameters are generally indirectly estimated from spaceborne sensors, involving complex retrieval algorithms. To ensure robustness in the observed behaviors, several data sets, originating from different retrievals and documenting a given parameter, are used for this study over the 2000–2012 period. The sample size is thus increased and the different retrieved parameters can be compared both in terms of climatology and at the event scale. One should keep in mind that inverting spaceborne observations in this geographical area at this season is challenging because relatively low cloud amount and water vapor amount are expected as well as a quite high level of atmospheric dust loading over nonvegetated surfaces (necessitating a good detection and accuracy of the retrieval algorithms).

The climatological behaviors (climatology being computed over the longest available data record) of the different parameters have been documented including the various data sets. In spring, a gradual increase in precipitable water is observed, the aerosol loading reaches its yearly maximum, the presence of clouds reduces the energy loss of the atmospheric system, and a maximum in incoming fluxes at the surface is concomitant with the highest maximum and minimum daily temperatures. For a given geophysical parameter, the available data sets can exhibit systematic differences even if they are based on the same retrieval algorithm. These differences are likely due to different sensor sensitivities, retrieval assumptions, or sampling time in the diurnal cycle. However, all of them are able to document the synoptic-scale variability of the atmosphere, as the use of anomalies with respect to the climatology removes most of the systematic differences between the data sets.

Two different HW categories are considered in this study, following the Barbier et al. (2018) definition: HW_{max} and HW_{min} events are detected based on T_{max} and T_{min}, respectively. The mean value of each atmospheric variables and their anomalies with respect to the climatological values are then computed for the whole spatial extent of each HW event day. Even if both types of events are identified on different temperature metrics, they both correspond to a daily mean temperature higher than its climatological value by about 2 K. The different processes that are likely to be at play in this temperature increase are summarized in Figure 14. Temperature anomalies are not directly related to anomalies in the incoming fluxes since processes can compensate each other during both types of HWs. Some robust signals emerge when individual processes are examined, in agreement with the results of Hong et al. (2018) over the Korea Peninsula. HW_{min} events are associated with positive anomalies of the incoming LW flux, consistent with an increase of both precipitable water and AOD. These latter positive anomalies in turns explain the negative anomalies found in the incoming SW flux, leading to very small anomalies in the total incoming fluxes. For HW_{max} events, a decrease in cloud cover is generally observed as well as a moderate decrease in AOD and eventually in precipitable water. They lead to an increase in the incoming SW flux, which contributes to generate the extreme daily temperature (Hong et al., 2018). The more intense HW_{max} are however found to be associated with a reinforced amount of humidity, suggesting a subcategory. Other processes, which have not been investigated here, may also contribute to the HW temperature increase, in particular dynamical processes that may advect warmer air over the Sahel.

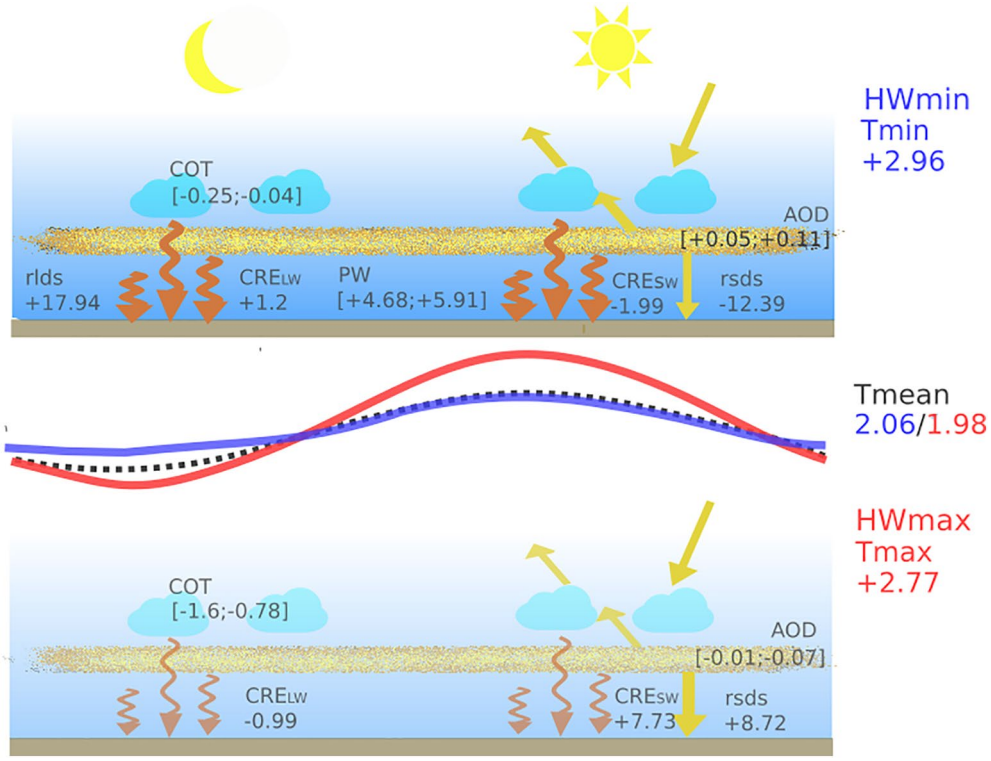

Figure 14. Schematic of the different processes at play during HW_{min} (top) and HW_{max} (bottom) events. Arrow thickness depicts the magnitude of SW (yellow) and LW (red) fluxes. Blue, red, and dotted black lines correspond to schematic diurnal evolution of the temperature for HW_{min}, HW_{max}, and climatology. Anomaly mean values (when significant, see Section 4) of the various parameters documented in this studies are superimposed. SW, shortwave; LW, longwave.

Further analysis of the relationships between the various atmospheric parameters and the temperature is needed in order to quantitatively explain the processes leading to the temperature anomaly. For this purpose, the use of a radiative transfer model fed with observations at particular well-instrumented location may be of particular interest and is left for future work.

Because all the parameters are difficult to be simultaneously observed, the approach proposed in this paper has not included a temporal dimension. The use of a model may help in the understanding of both types of HWs. In this perspective, the present documentation will be useful to evaluate the representativeness of the simulated events as well as the quality of the model. Such modeling effort is ongoing. As stressed in the introduction, the present study did not examine the synoptic situation in which the HW events occur. Such an analysis is needed, in particular to document and understand the mechanisms allowing the advection of water vapor over the Sahel during spring. Are there also particular dynamical situations that may advect warm temperatures during Sahelian HWs and that would reinforce the incoming LW fluxes (Miralles et al., 2014; Perkins, 2015)? Over the Korea Peninsula, Hong et al. (2018) find a positive anomaly of temperature advection at 300 hPa, in case of HW_{max}. The role of atmospheric wave pattern, occurring at different scales, deserves further attention, as, for instance, Rusticucci and Vargas (1995) or Campetella and Rusticucci (1998) show that HW occurrence over subtropical South America can be related to subsynoptic wave activity even if the high temperature persists longer than the wave activity. The end of the spring period sees the Sahel start to green. The land surface–atmosphere interaction may therefore change and in particular mitigate the HW magnitude. The role of the growing vegetation thus requires further investigation in the future.

The present study also offers an observational benchmark for General Circulation Model evaluation, in terms of both mean climatology and HW events over West Africa, and in particular with regards to the radiative budget at the surface and its various components.

Data Availability Statement

The BEST data were obtained from http://berkeleyearth.org/archive/data/. CERES SYN1deg data were obtained from the NASA Langley Research Center Atmospheric Science Data Center: https://ceres.larc.nasa.gov/data/#syn1deg-level-3. The Aqua and Terra/MODIS Aerosol Cloud Water Vapor Ozone Daily L3 Global 1 Deg. data set(s) were acquired from the Level-1 and Atmosphere Archive & Distribution System (LAADS) Distributed Active Archive Center (DAAC), located in the Goddard Space Flight Center in Greenbelt, MD (https://ladsweb.nascom.nasa.gov/). AERUS-GEO has been obtained from https://www.icare.univ-lille.fr/data-access/data-archive-access/?dir=GEO/MSG+0000/SEV_AERUS-AEROSOL-D3.v1.04. We thank Goddard Earth Sciences Data Information and Services Center for AIRS/AMSU data. AIRX3STD data (https://doi.org/10.5067/Aqua/AIRS/DATA301) were obtained through the Goddard Earth Sciences Data and Information Services Center (online at https://acdisc.gesdisc.eosdis.nasa.gov/data/Aqua_AIRS_Level3/AIRX3STD.006/).

Acknowledgments
This work is dedicated to Françoise Guichard memory who passed away on December 5, 2020, a couple of days before the submission of this paper. Up to this date, she was fully invested in Sahelian climate studies. She was at the initiative of this collective work and actively contributed to the elaboration of this paper. This study is part of ANR project ACASIS (2014–1017; grant ANR-13-SENV-0007). This work has also been partly supported by CNES. Bryan Vincent and Nicolas Mary who initiated this work during their internship at CNRM are acknowledged. This work was partly supported by CNES.

References

Agusti-Panareda, A., Beljaard, A., Cardinali, C., Genkova, I., & Thorncroft, C. D. (2010). Impact of assimilating AMMA soundings on ECMWF analyses and forecasts. *Weather and Forecasting*, *25*, 1142–1160.

Balkanski, Y., Schulz, M., Claquin, T., & Guibert, S. (2007). Reevaluation of Mineral aerosol radiative forcings suggests a better agreement with satellite and AERONET data. *Atmospheric Chemistry and Physics*, *7*, 81–95. https://doi.org/10.5194/acp-7-81-2007

Barbier, J., Guichard, F., Bouniol, D., Couvreux, F., & Roehrig, R. (2018). Detection of intraseasonal large-scale heat waves: Characteristics and historical trends during the Sahelian spring. *Journal of Climate*, *31*, 61–80. https://doi.org/10.1175/JCLI-D-17-0244.1

Blackwell, W. J. (2005). A neural-network technique for the retrieval of atmospheric temperature and moisture profiles from high spectral resolution sounding data. *IEEE Transactions on Geoscience and Remote Sensing*, *43*(11), 2535–2546. https://doi.org/10.1109/tgrs.2005.855071

Bock, O., Bouin, M.-N., Doerflinger, E., Collard, P., Masson, F., Meynadier, R., et al. (2008). West African Monsoon observed with ground-based GPS receivers during African Monsoon Multidisciplinary Analysis (AMMA). *Journal of Geophysical Research*, *113*, D21105. https://doi.org/10.1029/2008JD010327

Campetella, C., & Rusticucci, M. (1998). Synoptic analysis of an extreme heat spell over Argentina in March 1980. *Meteorological Applications*, *5*, 217–226. https://doi.org/10.1017/s1350482798000851

Carrer, D., Roujean, J.-L., Hautecoeur, O., & Elias, T. (2010). Daily estimates of aerosol optical thickness over land surface based on a directional and temporal analysis of SEVIRI MSG visible observations. *Journal of Geophysical Research*, *115*, D10208. https://doi.org/10.1029/2009JD012272

Caton Harrison, T., Washington, R., & Engelstaedter, S. (2019). A 14-year climatology of Saharan dust emission mechanisms inferred from automatically tracked plumes. *Journal of Geophysical Research: Atmospheres*, *124*, 9665–9690. https://doi.org/10.1029/2019JD030291

Cattiaux, J., Vautard, R., & Yiou, P. (2009). Origins of the extremely warm European fall of 2006. *Geophysical Research Letters*, *36*, L06713. https://doi.org/10.1029/2009GL037339

Couvreux, F., Guichard, F., Bock, O., Lafore, J.-P., & Redelsperger, J.-L. (2010). Monsoon flux pulsations over West Africa prior to the monsoon onset. *Quarterly Journal of the Royal Meteorological Society*, *136*(S1), 159–173. https://doi.org/10.1002/qj.473

Diallo, F. B., Hourdin, F., Rio, C., Traore, A.-K., Mellul, L., Guichard, F., & Kergoat, L. (2017). The surface energy budget computed at the grid-scale of a climate model challenged by station data in West Africa. *Journal of Advances in Modeling Earth Systems*, *9*, 2710–2738. https://doi.org/10.1002/2017MS001081

Doelling, D. R., Sun, M., Nguyen, L. T., Nordeen, M. L., Haney, C. O., Keyes, D. F., & Mlynczak, P. E. (2016). Advances in geostationary-derived longwave fluxes for the CERES synoptic (SYN1deg) product. *Journal of Atmospheric and Oceanic Technology*, *33*, 503–521. https://doi.org/10.1175/JTECH-D-15-0147.1

Fink, A. H., Engel, T., Ermert, V., van der Linden, R., Schneidewind, M., Redl, R., et al. (2017). Mean climate and seasonal cycle. In *Meteorology of tropical West Africa: The forecasters' handbook* (pp. 1–39). https://doi.org/10.1002/9781118391297.ch1

Fontaine, B., Janicot, S., & Monerie, P.-A. (2013). Recent changes in air temperature, heat waves occurrences and atmospheric circulation in northern Africa. *Journal of Geophysical Research: Atmospheres*, *118*, 536–552. https://doi.org/10.1002/jgrd.50667

Formenti, P., Rajot, J. L., Desboeufs, K., Caquineau, S., Chevaillier, S., Nava, S., et al. (2008). Regional variability of the composition of mineral dust from western Africa: Results from the AMMA SOP0/DABEX and DODO field campaigns. *Journal of Geophysical Research*, *113*, D00C13. https://doi.org/10.1029/2008JD009903

Gruhier, C., de Rosnay, P., Kerr, Y., Mougin, E., Ceschia, E., Calvet, J.-C., & Richaume, P. (2008). Evaluation of AMSR-E soil moisture product based on ground measurements over temperate and semi-arid regions. *Geophysics Research Letters*, *35*, L10405. https://doi.org/10.1029/2008GL033330

Guichard, F., Kergoat, L., Mougin, E., Timouk, F., Baup, F., Hiernaux, P., & Lavenu, F. (2009). Surface thermodynamics and radiative budget in the Sahelian Gourma: Seasonal and diurnal cycles. *Journal of Hydrology*, *375*(1–2), 161–177. https://doi.org/10.1016/j.jhydrol.2008.09.007

Haywood, J. M., Pelon, J., Formenti, P., Bharmal, N., Brooks, M., Capes, G., et al. (2008). Overview of the dust and biomass-burning experiment and African monsoon multidisciplinary analysis special observing Period-0. *Journal of Geophysical Research*, *113*, D00C17. https://doi.org/10.1029/2008JD010077

Heinold, B., Knippertz, P., Marsham, J. H., Fiedler, S., Dixon, N., Schepanski, K., et al. (2013). The role of deep convection and low-level jets for dust emission in summertime West Africa. *Journal of Geophysical Research*, *118*, 1–16. https://doi.org/10.1002/jgrd.50402

Hill, P. G., Allan, R. P., Chiu, J. C., & Stein, T. H. M. (2016). A multi-satellite climatology of clouds, radiation, and precipitation in southern West Africa and comparison to climate models. *Journal of Geophysical Research: Atmospheres*, *121*, 10857–10879. https://doi.org/10.1002/2016JD025246

Hong, J.-S., Yeh, S.-W., & Seo, K.-H. (2018). Diagnosing physical mechanisms leading to pure heat waves versus pure tropical nights over the Korean Peninsula. *Journal of Geophysical Research: Atmospheres*, *123*, 7149–7160. https://doi.org/10.1029/2018JD028360

Hsu, N. C., Tsay, S.-C., King, M. D., & Herman, J. R. (2004). Aerosol properties over bright-reflecting source regions. *IEEE Transactions on Geoscience and Remote Sensing*, *42*(3), 557–569. https://doi.org/10.1109/TGRS.2004.824067

Kang, H.-J., Yoo, J.-M., Jeong, M.-J., & Won, Y.-I. (2005). Uncertainties of satellite-derived surface skin temperatures in the polar oceans: MODIS, AIRS/AMSU, and AIRS only. *Atmospheric Measurement Techniques*, *8*, 4025–4041.

Kato, S., Loeb, N. G., Rose, F. G., Doelling, D. R., Rutan, D. A., Caldwell, T. E., et al. (2013). Surface irradiances consistent with CERES-derived top-of-atmosphere shortwave and longwave irradiances. *Journal of Climate*, *26*, 2719–2740. https://doi.org/10.1175/JCLI-D-12-00436.1

Kaufman, Y. J., Tanré, D., Remer, L. A., Vermote, E. F., Chu, A., & Holben, B. N. (1997). Operational remote sensing of tropospheric aerosol over land from EOS moderate resolution imaging spectroradiometer. *Journal of Geophysical Research*, *102*(D14), 17051–17067. https://doi.org/10.1029/96JD03988

King, M. D., Menzel, W. P., Kaufman, Y. J., Tanré, D., Gao, B.-C., Platnick, S., et al. (2003). Cloud and aerosol properties, precipitable water, and profiles of temperature and water vapor from MODIS. *IEEE Transactions on Geoscience and Remote Sensing*, *41*(2), 442–458. https://doi.org/10.1109/tgrs.2002.808226

Largeron, Y., Guichard, F., Roehrig, R., Couvreux, F., & Barbier, J. (2020). The April 2010 North African heatwave: When water vapor greenhouse effect drives nighttime temperatures. *Climate Dynamics*, *54*, 3879–3905. https://doi.org/10.1007/s00382-020-05204-7

Loeb, N., Doelling, D. R., Wang, H., Su, W., NGuyen, C., Corbett, J. G., et al. (2018). Clouds and the Earth's Radiant Energy System (CERES) energy balanced and filled (EBAF) top-of-atmosphere (TOA) edition-4.0 data Product. *Journal of Climate*, *31*, 895–918. https://doi.org/10.1175/JCLI-D-17-0208.1

Mallet, M., Tulet, P., Serça, D., Solmon, F., Dubovik, O., Pelon, J., et al. (2009). Impact of dust aerosols on the radiative budget, surface heat fluxes, heating rate profiles and convective activity over West Africa during March 2006. *Atmospheric Chemistry and Physics*, *9*, 7143–7160. https://doi.org/10.5194/acp-9-7143-2009

Marsham, J. H., Parker, D. J., Todd, M. C., Banks, J. R., Brindley, H. E., Garcia-Carreras, L., et al. (2016). The contrasting roles of water and dust in controlling daily variations in radiative heating of the summertime Saharan heat low. *Atmospheric Chemistry and Physics*, *16*, 3563–3575. https://doi.org/10.5194/acp-16-3563-2016

Marticorena, B., Chatenet, B., Rajot, J.-L., Traoré, S., Coulibaly, M., Diallo, A., et al. (2010). Temporal variability of mineral dust concentrations over West Africa: Analyses of a pluriannual monitoring from the AMMA Sahelian Dust Transect. *Atmospheric Chemistry and Physics*, *10*, 8899–8915. https://doi.org/10.5194/acp-10-8899-2010

Meehl, G. A., & Tebaldi, C. (2004). More intense, more frequent, and longer lasting heat waves in the 21st century. *Science*, *305*, 994–997. https://doi.org/10.1126/science.1098704

Miller, M. A., Ghate, V. P., & Zahn, R. K. (2012). The radiation budget of the West African Sahel and its controls: A perspective from observations and global climate models. *Journal of Climate*, *25*, 5976–5996. https://doi.org/10.1175/JCLI-D-11-00072.1

Milton, S. F., Greed, G., Brooks, M. E., Haywood, J., Johnson, B., Allan, R. P., et al. (2008). Modeled and observed atmospheric radiation balance during the West African dry season: Role of mineral dust, biomass burning aerosol, and surface albedo. *Journal of Geophysical Research*, *113*, D00C02. https://doi.org/10.1029/2007JD009741

Minnis, P., Sun-Mack, S., Young, D. F., Heck, P. W., Garber, D. P., Chen, Y., et al. (2011). CERES edition-2 cloud property retrievals using TRMM VIRS and Terra and Aqua MODIS data—Part I: Algorithms. *IEEE Transactions on Geoscience and Remote Sensing*, *49*, 4374–4400. https://doi.org/10.1109/TGRS.2011.2144601

Miralles, D. G., Teuling, A. J., van Heerwaarden, C. C., & de Arellano, J. V. G. (2014). Mega-heatwave temperatures due to combined soil desiccation and atmospheric heat accumulation. *Nature Geoscience*, *7*(5), 345–349. https://doi.org/10.1038/ngeo2141

Mougin, E., Hiernaux, P., Kergoat, L., Grippa, M., de Rosnay, P., Timouk, F., et al. (2009). The AMMA-CATCH Gourma observatory site in Mali: Relating climatic variations to changes in vegetation, surface hydrology, fluxes and natural resources. *Journal of Hydrology*, *375*, 14–33. https://doi.org/10.1016/j.jhydrol.2009.06.045

Niang, I., Ruppel, O. C., Abdrabo, M. A., Essel, A., Lennard, C., Padgham, J., & Urquhart, P. (2014). Africa. In *Climate change 2014: Impacts, adaptation, and vulnerability. Part B: Regional aspects. Contribution of Working Group II to the fifth assessment report of the Intergovernmental Panel on Climate Change*. Cambridge, UK: Cambridge University Press.

Oueslati, B., Pohl, B., Moron, V., Rome, S., & Janicot, S. (2017). Characterization of heat waves in the Sahel and associated mechanisms. *Journal of Climate*, *30*, 3095–3115. https://doi.org/10.1175/jcli-d-16-0432.1

Pagès, J.-P., Frangi, J.-P., Durand, P., Estournel, C., & Druilhet, A. (1988). Etude de la couche limite de surface sahelienne—Experience Yantala. *Boundary-Layer Meteorology*, *43*, 183–203. https://doi.org/10.1007/bf00153979

Parker, T. J., Berry, G. J., & Reeder, M. J. (2014). The structure and evolution of heat waves in southeastern Australia. *Journal of Climate*, *27*(15), 5768–5785. https://doi.org/10.1175/JCLI-D-13-00740.1

Parker, T. J., Berry, G. J., Reeder, M. J., & Nicholls, N. N. (2014). Modes of climate variability and heat waves in Victoria, southeastern Australia. *Geophysical Research Letters*, *41*, 6926–6934. https://doi.org/10.1002/2014GL061736

Perkins, S. E. (2015). A review on the scientific understanding of heatwaves—Their measurement, driving mechanisms, and changes at the global scale. *Journal of Atmospheric Research*, *164*, 242–267. https://doi.org/10.1016/j.atmosres.2015.05.014

Pierre, C., Bergametti, G., Marticorena, B., Abdourhamane Tourré, A., Rajot, J.-L., & Kergoat, L. (2014). Modeling wind erosion flux and its seasonality from a cultivated Sahelian surface: A case study in Niger. *Catena*, *122*, 61–71. https://doi.org/10.1016/j.catena.2014.06.006

Platnick, S. E., Meyer, K. G., King, M. D., Wind, G., Amarasinghe, N., Marchant, B., et al. (2017). The MODIS cloud optical and microphysical products: Collection 6 updates and examples from Terra and Aqua. *IEEE Transactions on Geoscience and Remote Sensing*, *55*(1), 502–525. https://doi.org/10.1109/TGRS.2016.2610522

Prata, A. J. (1996). A new long-wave formula for estimating downward clear-sky radiation at the surface. *Quarterly Journal of the Royal Meteorological Society*, *122*, 1127–1151. https://doi.org/10.1002/qj.49712253306

Prospero, J. M., Ginoux, P., Torres, O., Nicholson, S., & Gill, T. E. (2002). Environmental characterization of global sources of atmospheric soil dust identified with the nimbus 7 total ozone mapping spectrometer (TOMS) absorbing aerosol product. *Reviews of Geophysics*, *40*(1), 1002. https://doi.org/10.1029/2000RG000095

Quinting, J. F., & Reeder, M. J. (2017). Southeastern Australian heat waves from a trajectory viewpoint. *Monthly Weather Review*, *145*, 4109–4125. https://doi.org/10.1175/MWR-D-17-0165.1

Rao, Y., Liang, S., & Yue, Y. (2018). Land surface air temperature data are considerably different among BEST-LAND, CRU-TEM4v, NASA-GISS, and NOAA-NCEI. *Journal of Geophysical Research*, *123*, 5881–5900. https://doi.org/10.1029/2018JD028355

Remer, L. A., Kaufman, Y. J., Tanré, D., Mattoo, S., Chu, D. A., Martins, J. V., et al. (2005). The MODIS aerosol algorithm, products, and validation. *Journal of the Atmospheric Sciences*, *62*, 947–973. https://doi.org/10.1175/JAS3385.1

Rohde, R., Muller, R., Jacobsen, R., Perlmutter, S., Rosenfeld, A., Wurtele, J., et al. (2013). Berkeley earth temperature averaging process. *Geoinformatics & Geostatistics: An Overview*, *13*, 20–100.

Rohde, R., Muller, R. A., Jacobsen, R., Muller, E., Perlmutter, S., Rosenfeld, A., et al. (2014). A new estimate of the average earth surface land temperature spanning 1753 to 2011. *Geoinformatics & Geostatistics: An Overview*, *1*, 1. https://doi.org/10.4172/2327-4581.1000101

Rusticucci, M., & Vargas, W. (1995). Synoptic situations related to spells of extreme temperatures over Argentina. *Meteorological Applications*, *2*, 291–300.

Rutan, D. A., Kato, S., Doelling, D. R., Rose, F. G., Nguyen, L. T., Caldwell, T. E., & Loeb, N. G. (2015). CERES synoptic product: Methodology and validation of surface radiant flux. *Journal of Atmospheric and Oceanic Technology*, *32*, 1121–1143. https://doi.org/10.1175/JTECH-D-14-00165.1

Seluchi, M. E., Norte, F. A., Gomes, J. L., & Simonelli, S. (2006). *Synoptic and thermodynamic analysis of an extreme heat wave over subtropical South America*. Paper presented at Proceedings of 8 ICSHMO, Foz do Iguaçu, Brazil, April 24–28, 2006, INPE.

Slingo, A., White, H. E., Bharmal, N. A., & Robinson, G. J. (2009). Overview of observations from the RADAGAST experiment in Niamey, Niger: 2. Radiative fluxes and divergences. *Journal of Geophysical Research*, *114*, D00E04. https://doi.org/10.1029/2008JD010497

Tanré, D., Kaufman, Y. J., Herman, M., & Mattoo, S. (1997). Remote sensing of aerosol properties over oceans using the MODIS/EOS spectral radiances. *Journal of Geophysical Research*, *102*(D14), 16971–16988. https://doi.org/10.1029/96JD03437

Tao, M., Chen, L., Wang, Z., Wang, J., Wang, W., Tao, J., et al. (2017). Evaluation of MODIS Deep Blue aerosol algorithm in desert region of East Asia: Ground validation and intercomparison. *Journal of Geophysical Research*, *122*, 10357–10368. https://doi.org/10.1002/2017JD026976

Wielicki, B. A., Barkstrom, B. R., Harrison, E. F., Lee, R. B., III, Smith, G. L., & Cooper, J. E. (1996). Clouds and the Earth's Radiant Energy System (CERES): An earth observing system experiment. *Bulletin of the American Meteorological Society*, *77*, 853–868. https://doi.org/10.1175/1520-0477(1996)077<0853:CATERE>2.0.CO;2

Yang, E.-S., Gupta, P., & Sundar, A. C. (2009). Net radiative effect of dust aerosols from satellite measurements over Sahara. *Geophysical Research Letters*, *36*, L18812. https://doi.org/10.1029/2009GL039801

Zhang, T., Hoerling, M. P., Perlwitz, J., Sun, D.-Z., & Murray, D. (2011). Physics of U.S. surface temperature response to ENSO. *Journal of Climate*, *24*, 4874–4887. https://doi.org/10.1175/2011JCLI3944.1